Broadband Electromagnetic Modeling of On-Chip Passives Using a Differential Surface Admittance Operator for 3-D Piecewise Homogeneous Structures

Tim Pattyn, *Student Member, IEEE*, Xiao Sun, *Member, IEEE*, Eric Beyne, *Senior Member, IEEE*, Daniël De Zutter, *Life Fellow, IEEE*, Martijn Huynen, *Member, IEEE* and Dries Vande Ginste, *Senior Member, IEEE*

***Abstract*—Accurate modeling of on-chip passive components is vital for reliable integrated circuit design. However, this is non-trivial due to the inherent heterogeneity of the structures and the wide range of material parameters involved. In this work, we present a single-source boundary integral equation (BIE) for modeling on-chip interconnects and passive elements. To reduce the number of discretization elements — and thus the number of unknowns — we construct a 3-D differential surface admittance (DSA) operator for piecewise homogeneous cuboidal and rectilinear polyhedral objects. Specifically, a novel method is proposed to handle material interfaces efficiently. By combining this new formulation of the DSA operator with the augmented electric field integral equation, we obtain a framework that enables accurate modeling and fast broadband impedance extraction of on-chip structures. The proposed approach is validated through several numerical experiments, including important applications such as metal-insulator-metal (MIM) capacitors, and demonstrates excellent agreement with reference solutions while significantly reducing computational cost compared to state-of-the-art solvers.**

***Index Terms*—3-D differential surface admittance (DSA) operator, material interfaces, on-chip passives, piecewise homogeneous media, single-source boundary integral equation (BIE)**

I. Introduction

THE demand for global connectivity has driven rapid advancements in communication systems and the rise of the Internet of Things (IoT). This has led to increasingly complex printed circuit boards (PCBs) and integrated circuits (ICs) as devices shrink and operate at higher frequencies. Consequently, signal integrity issues — stemming from, e.g., skin effect, self-resonance and crosstalk [1] — which disrupt proper circuit performance, become more prevalent. Hence, electromagnetic (EM) solvers have become essential for accurately modeling and optimizing interconnects and passive elements, making them critical tools in modern electronic design.

A plethora of full-wave solvers has been described in literature. Generally they can be subdivided into two main categories. On the one hand, volumetric solvers tackle the problem by meshing the full volume and approximating the fields on this mesh. Some well-known types are the finite-element methods (FEM) [2], volume integral equation (VIE) methods [3]–[5] and the class of partial-element equivalent circuit (PEEC) methods [6], [7]. On the other hand, boundary integral equation (BIE) methods only mesh the surface of the considered volumes, significantly reducing the overall matrix size at the cost of higher computational complexity. The Poggio-Miller-Chan-Harrington-Wu-Tsai (PMCHWT) formulation [8] is a general method for simulating piecewise homogeneous bodies, but struggles with good conductors due to challenges in evaluating the Green's function in conducting materials subject to strong skin effect. Although techniques exist to mitigate this issue [9], the PMCHWT method still faces challenges in the presence of high dielectric contrast [10]. Other methods, like N-Müller [11], avoid these concerns but may suffer from accuracy problems, especially for non-smooth objects [12]. Alternative approaches remove material contrast by replacing the material of an object with the background medium and imposing a suitable boundary condition, of which the surface impedance or Leontovich boundary condition [13] is a well-known example. While effective for planar surfaces, it is only valid as long as the dielectric contrast and radius of curvature are sufficiently large [14]. The global impedance boundary condition (GIBC) addresses these limitations [15], [16], but faces difficulties with the accurate evaluation of singular integrals.

In the realm of single-source BIE methods, the differential surface admittance (DSA) operator has been described as an alternative solution [17]. This operator facilitates replacing the material with the background medium by introducing a fictitious surface current density $\mathbf{j_s}$ on the object's surface $\mathcal{S}$, as depicted in Fig. 1. The current density $\mathbf{j_s}$ is determined as follows:

$$\mathbf{j}_s = \hat{\mathbf{n}} \times (\mathbf{h} - \mathbf{h}') = (\mathcal{P} - \mathcal{P}_0)\mathbf{e}_0^t = \mathcal{Y}\mathbf{e}_0^t, \tag{1}$$

with $\mathbf{e_0^t}$ the tangential electric field on $\mathcal{S}$ and $\mathcal{Y}$ the pertinent DSA operator. This DSA operator can be interpreted as the difference between the Poincaré-Steklov (PS) operators $\mathcal{P}$ and $\mathcal{P}_0$, mapping the tangential electric field on $\mathcal{S}$ onto the rotated tangential magnetic field on $\mathcal{S}$ for the situations in Fig. 1a and 1b, respectively. Initially formulated for 2-D sim-

This work was supported by the Research Foundation–Flanders (FWO) under Grant 1S04425N.

T. Pattyn, D. De Zutter, M. Huynen and D. Vande Ginste are with Quest/IDLab, Department of Information Technology, Ghent University-imec, 9052 Ghent, Belgium (e-mail: tim.pattyn@ugent.be; daniel.dezutter@ugent.be; martijn.huynen@ugent.be; dries.vandeginste@ugent.be).

X. Sun and E. Beyne are with imec, 3001 Leuven, Belgium (e-mail: xiao.sun@imec.be; eric.beyne@imec.be).

ulations, several approaches have been proposed in literature to derive the relevant $\mathcal{Y}$-operator. In [17], [18], analytical expressions for the eigenfunctions of the considered 2-D volumes are exploited in the derivation of the DSA operator. An extension to arbitrary 2-D objects was developed based on a contour integral method [19], requiring the Green's function inside the material. The authors of [20] expanded the latter approach to composite 2-D volumes. More recently, an alternative methodology has been proposed for arbitrary polygons based on the Fokas method [21]. This method proves very efficient, as it entirely removes the need to evaluate Green's functions associated with the inner material. Moreover, in [22], it is shown that combined dielectric and magnetic contrast is accurately captured by employing rooftop basis functions instead of pulse basis functions.

Over the last years, the DSA formalism has been extended to 3-D volumes, i.e., cylinders [23], [24] and cuboids [25], [26], by leveraging the analytical expressions for the eigenmodes of these objects. Alternatively, a surface integral method can be adopted to derive the 3-D operator [27], relying on the traditional Green's function-based BIE operators.

However, so far, incorporating composite (3-D) objects within the single-source BIE formulation remains challenging. Current 3-D DSA formulations do not allow inclusion of piecewise homogeneous materials, as sketched in Fig. 2a, without introducing a surface current density at the interface between the two homogeneous volumes $\mathcal{V}_1$ and $\mathcal{V}_2$. In [26], infinitesimally small wires are used to connect the two adjacent volumes, which introduces additional unknowns while still requiring the current density on the material interface. Furthermore, this method is limited to good conducting materials ($\sigma \gg \omega\epsilon$). The authors of [28] propose an alternative approach. The junction problem is bypassed by introducing an infinitesimally small gap between $\mathcal{V}_1$ and $\mathcal{V}_2$. Next, they rely on the Combined Field Integral Equation (CFIE) operator to treat the material interface. This method also still requires a surface current density on the material interface, resulting in additional unknowns. Moreover, the CFIE operator demands non-trivial testing procedures and is also computationally more expensive compared to alternative formulations such as the Electric Field Integral Equation (EFIE) [29].

Therefore, in this work, we present a new 3-D DSA-operator-based method to accurately and efficiently model piecewise homogeneous cuboidal and rectilinear polyhedral objects, which constitute on-chip interconnects and passive components. The proposed technique does not introduce surface current densities on the inner material interfaces, thereby significantly reducing the number of unknowns. Moreover, it remains compatible with traditional single-source EFIE formulations.

The remainder of this paper is organized as follows. Section II derives the DSA operator for a piecewise homogeneous cuboid, starting from the entire domain basis function (EDBF) expansion proposed in [26]. Section III extends this formulation to piecewise homogeneous rectilinear polyhedra. In Section IV-A, we briefly discuss the generalization to arbitrary piecewise homogeneous volumes. Section V describes how the DSA operator is integrated with the EFIE to solve the exterior

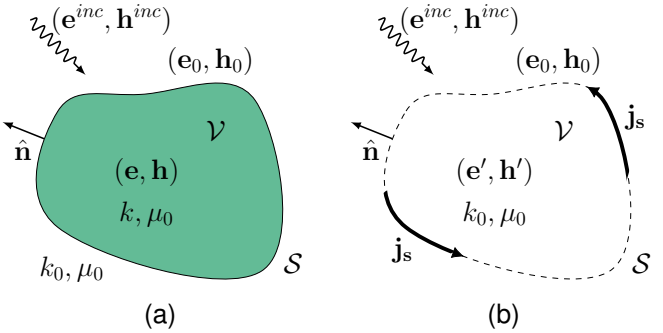

Fig. 1. Geometry of the problem: (a) Homogeneous volume $\mathcal{V}$ with boundary surface $\mathcal{S}$ placed inside a background medium. In (b), a surface current $\mathbf{j}_s$ is introduced on $\mathcal{S}$ and the inner material is replaced by the background medium.

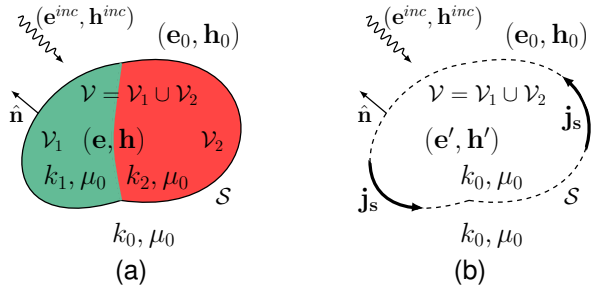

Fig. 2. Geometry of the problem: (a) Piecewise homogeneous volume $\mathcal{V} = \mathcal{V}_1 \cup \mathcal{V}_2$ with boundary surface $\mathcal{S}$ placed inside a background medium. In (b), a surface current $\mathbf{j}_s$ is introduced on $\mathcal{S}$ and the inner materials are replaced by the background medium.

problem. Following the theoretical derivations, Section VI presents a thorough validation of our novel method against state-of-the-art solvers, demonstrating its accuracy and efficiency. Moreover, its applicability is highlighted by extracting the broadband impedance response of state-of-the-art on-chip metal-insulator-metal (MIM) capacitors. Finally, Section VII concludes the paper.

II. DSA Operator for Piecewise Homogeneous Cuboids

A. Entire Domain Formulation for Homogeneous Cuboids

In the general definition of the $\mathcal{Y}$-operator (1), the PS operators $\mathcal{P}$ and $\mathcal{P}_0$, corresponding to Fig. 1a and 1b respectively, are continuous. By expanding the tangential electric and magnetic fields on $\mathcal{S}$ in basis functions, the PS operators become matrices relating the expansion coefficients of the rotated tangential magnetic field to those of the tangential electric field. For homogeneous cuboidal objects, dedicated entire domain basis functions (EDBFs) were introduced in [26]. These EDBFs stem from the field expressions for the transverse electric (TE) and transverse magnetic (TM) modes of a cuboidal cavity. The relevant expressions are concisely repeated below for convenience. The reader is referred to [26] for more details. The TE and TM modes of a cuboidal cavity with dimensions $\{l_x, l_y, l_z\}$ are given by:

$$\mathbf{e}_{TE,mnp} = k_{mnp}\lambda_y \cos(\lambda_x x)\sin(\lambda_y y)\sin(\lambda_z z)\hat{\mathbf{x}} - k_{mnp}\lambda_x \sin(\lambda_x x)\cos(\lambda_y y)\sin(\lambda_z z)\hat{\mathbf{y}} \quad (2)$$

$$\mathbf{h}_{TE,mnp} = \lambda_z\lambda_x \sin(\lambda_x x)\cos(\lambda_y y)\cos(\lambda_z z)\hat{\mathbf{x}} + \lambda_z\lambda_y \cos(\lambda_x x)\sin(\lambda_y y)\cos(\lambda_z z)\hat{\mathbf{y}} - (\lambda_x^2+\lambda_y^2)\cos(\lambda_x x)\cos(\lambda_y y)\sin(\lambda_z z)\hat{\mathbf{z}} \quad (3)$$

$$\mathbf{e}_{TM,mnp} = -\lambda_z\lambda_x \cos(\lambda_x x)\sin(\lambda_y y)\sin(\lambda_z z)\hat{\mathbf{x}} + \lambda_z\lambda_y \sin(\lambda_x x)\cos(\lambda_y y)\sin(\lambda_z z)\hat{\mathbf{y}} + (\lambda_x^2+\lambda_y^2)\sin(\lambda_x x)\sin(\lambda_y y)\cos(\lambda_z z)\hat{\mathbf{z}} \quad (4)$$

$$\mathbf{h}_{TM,mnp} = k_{mnp}\lambda_y \sin(\lambda_x x)\cos(\lambda_y y)\cos(\lambda_z z)\hat{\mathbf{x}} - k_{mnp}\lambda_x \cos(\lambda_x x)\sin(\lambda_y y)\cos(\lambda_z z)\hat{\mathbf{y}}, \quad (5)$$

with $\lambda_x = m\pi/l_x$, $\lambda_y = n\pi/l_y$, $\lambda_z = p\pi/l_z$ and $k_{mnp}^2 = \lambda_x^2+\lambda_y^2+\lambda_z^2$. These modes are projected onto each of the six faces of the cuboid since we are only interested in the tangential component of the electric and magnetic field on $\mathcal{S}$. The resulting expressions all show a similar form, leading to the following definition of the EDBFs for the cuboid:

$$\mathbf{f}_{u_q,u_l}(q,l) = \sin(\lambda_q q)\cos(\lambda_l l)\hat{\mathbf{l}}, \quad (6)$$

where q and l can be x, y or z with $q \neq l$, $\hat{\mathbf{l}}$ is the unit vector along the direction l and u_l is the subindex related to λ_l. For example, if $l = x$, then $\hat{\mathbf{l}} = \hat{\mathbf{x}}$ and $u_l = m$. The current density $\mathbf{j}_s$ and tangential electric field $\mathbf{e}_t$ on the top or bottom face, perpendicular to the x-axis, are expanded in EDBFs as follows:

$$\mathbf{e}_t = \sum_{np}(a_{np}^z \mathbf{f}_{n,p}(y,z) + a_{np}^y \mathbf{f}_{p,n}(z,y)) \quad (7)$$

$$\mathbf{j}_s = \sum_{np}(b_{np}^z \mathbf{f}_{n,p}(y,z) + b_{np}^y \mathbf{f}_{n,p}(z,y)), \quad (8)$$

with similar expressions for the other faces of the cuboid. Collecting all the electric field expansion coefficients, such as a_{np}^z and a_{np}^y in (7), from all six faces into the column vector $\bar{\mathbf{e}}_t$, and similarly collecting the fictitious surface current density coefficients, such as b_{np}^z and b_{np}^y in (8), into the vector $\bar{\mathbf{j}}_s$, results in the following relation between both vectors:

$$\bar{\mathbf{j}}_s = \bar{\bar{\mathcal{Y}}} \cdot \bar{\mathbf{e}}_t = (\bar{\bar{\mathcal{P}}} - \bar{\bar{\mathcal{P}}}_0) \cdot \bar{\mathbf{e}}_t, \quad (9)$$

where the matrix $\bar{\bar{\mathcal{Y}}}$ is the sought-after discretized DSA operator for a homogeneous cuboid expressed in terms of EDBFs. This specific choice of basis functions enables analytical determination of the elements of the discretized PS matrices $\bar{\bar{\mathcal{P}}}$ and $\bar{\bar{\mathcal{P}}}_0$ for the original and equivalent situation, respectively, and consequently also of $\bar{\bar{\mathcal{Y}}}$.

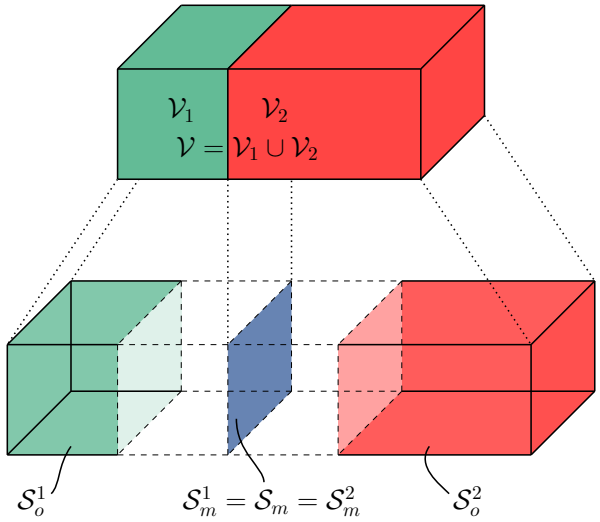

Fig. 3. Example of a piecewise homogeneous cuboid $\mathcal{V}$ consisting of two homogeneous volumes $\mathcal{V}_1$ and $\mathcal{V}_2$ with wavenumbers k_1 and k_2 respectively. The surface of $\mathcal{V}_1$ is called $\mathcal{S}^1 = \mathcal{S}_o^1 \cup \mathcal{S}_m$; similarly the surface of $\mathcal{V}_2$ is defined as $\mathcal{S}^2 = \mathcal{S}_o^2 \cup \mathcal{S}_m$. The total cuboid $\mathcal{V}$ has a boundary surface $\mathcal{S} = \mathcal{S}_o^1 \cup \mathcal{S}_o^2$.

B. Entire Domain Formulation for Piecewise Homogeneous Cuboids

To deal with the challenges outlined in the Introduction, we now derive a DSA operator for piecewise homogeneous, cuboidal objects without introducing surface current densities on the inner interfaces. Therefore, consider the piecewise homogeneous cuboid $\mathcal{V}$, shown in Fig. 3, with bounding surface $\mathcal{S} = \mathcal{S}_o^1 \cup \mathcal{S}_o^2$. The homogeneous sections of $\mathcal{V}$ are called $\mathcal{V}_1$ and $\mathcal{V}_2$ with boundary surfaces $\mathcal{S}^1 = \mathcal{S}_o^1 \cup \mathcal{S}_m$ and $\mathcal{S}^2 = \mathcal{S}_o^2 \cup \mathcal{S}_m$, respectively. The EDBF expansion of the previous section is exploited to construct the sought-after DSA operator.

In a first step, we impose continuity of the tangential magnetic and electric field on the inner interface $\mathcal{S}_m$ between the two materials inside $\mathcal{V}$. On this interface $\mathcal{S}_m$, the EDBFs of both volumes $\mathcal{V}_1$ and $\mathcal{V}_2$ are mutually orthogonal owing to their trigonometric nature. Therefore, the required field continuity is straightforwardly enforced on a function-by-function basis, explaining our choice of basis functions. To this end, we collect the entire domain expansion coefficients for the tangential electric field in column vectors $\bar{\mathbf{e}}^1$ and $\bar{\mathbf{e}}^2$ and for the rotated tangential magnetic field in column vectors $\bar{\mathbf{h}}^1$ and $\bar{\mathbf{h}}^2$, for $\mathcal{V}_1$ and $\mathcal{V}_2$ respectively. This yields:

$$\bar{\mathbf{h}}^1 = \bar{\bar{\mathcal{P}}}^1 \bar{\mathbf{e}}^1 \quad (10)$$

$$\bar{\mathbf{h}}^2 = \bar{\bar{\mathcal{P}}}^2 \bar{\mathbf{e}}^2, \quad (11)$$

where $\bar{\bar{\mathcal{P}}}^1$ and $\bar{\bar{\mathcal{P}}}^2$ are the PS matrices for the homogeneous volumes $\mathcal{V}_1$ and $\mathcal{V}_2$ respectively. To clearly distinguish between the tangential electric field expansion coefficients associated with the inner material interface $\mathcal{S}_m$ and those related to the other faces $\mathcal{S}_o^i$ $(i = 1, 2)$ of the cuboids, we may collect them separately in the column vectors $\bar{\mathbf{e}}^{i,m}$ and $\bar{\mathbf{e}}^{i,o}$ $(i = 1, 2)$, respectively. Following a similar procedure

for the rotated tangential magnetic field expansion coefficients allows us to cast (10) and (11) in the following block-matrix form:

$$\begin{bmatrix}\bar{\mathbf{h}}^{1,o}\\ \bar{\mathbf{h}}^{1,m}\end{bmatrix} = \begin{bmatrix}\bar{\bar{\mathcal{P}}}^{1,oo} & \bar{\bar{\mathcal{P}}}^{1,om}\\ \bar{\bar{\mathcal{P}}}^{1,mo} & \bar{\bar{\mathcal{P}}}^{1,mm}\end{bmatrix}\cdot\begin{bmatrix}\bar{\mathbf{e}}^{1,o}\\ \bar{\mathbf{e}}^{1,m}\end{bmatrix} \tag{12}$$

$$\begin{bmatrix}\bar{\mathbf{h}}^{2,o}\\ \bar{\mathbf{h}}^{2,m}\end{bmatrix} = \begin{bmatrix}\bar{\bar{\mathcal{P}}}^{2,oo} & \bar{\bar{\mathcal{P}}}^{2,om}\\ \bar{\bar{\mathcal{P}}}^{2,mo} & \bar{\bar{\mathcal{P}}}^{2,mm}\end{bmatrix}\cdot\begin{bmatrix}\bar{\mathbf{e}}^{2,o}\\ \bar{\mathbf{e}}^{2,m}\end{bmatrix}, \tag{13}$$

where the elements of the PS matrices $\bar{\bar{\mathcal{P}}}^1$ and $\bar{\bar{\mathcal{P}}}^2$ are ordered accordingly, leading to the 2×2 block structures. Each block is denoted by a superscript that is both appropriate and self-explanatory. Using the same number and ordering of EDBFs to expand the rotated tangential magnetic fields $\hat{\mathbf{n}}\times\mathbf{h}_1$ and $\hat{\mathbf{n}}\times\mathbf{h}_2$ (associated with $\mathcal{V}_1$ and $\mathcal{V}_2$ respectively) on the interface $\mathcal{S}_m$, the field continuity condition is expressed as:

$$\begin{aligned}\bar{\mathbf{h}}^{1,m}+\bar{\mathbf{h}}^{2,m} &= \bar{\bar{\mathcal{P}}}^{1,mm}\bar{\mathbf{e}}^{1,m}+\bar{\bar{\mathcal{P}}}^{1,mo}\bar{\mathbf{e}}^{1,o}\\ &\quad+\bar{\bar{\mathcal{P}}}^{2,mm}\bar{\mathbf{e}}^{2,m}+\bar{\bar{\mathcal{P}}}^{2,mo}\bar{\mathbf{e}}^{2,o}\\ &= 0,\end{aligned} \tag{14}$$

where the plus sign in the l.h.s. of (14) stems from the fact that the outward pointing normal vectors $\hat{\mathbf{n}}$, pertaining to $\mathcal{V}_1$ and $\mathcal{V}_2$, point in opposite directions on $\mathcal{S}_m$. Similarly, using also the same number and ordering of EDBFs to expand the tangential electric field, continuity at the interface $\mathcal{S}_m$ leads to $\bar{\mathbf{e}}^m=\bar{\mathbf{e}}^{1,m}=\bar{\mathbf{e}}^{2,m}$. Consequently, (14) reduces to:

$$(\bar{\bar{\mathcal{P}}}^{1,mm}+\bar{\bar{\mathcal{P}}}^{2,mm})\bar{\mathbf{e}}^m+\bar{\bar{\mathcal{P}}}^{1,mo}\bar{\mathbf{e}}^{1,o}+\bar{\bar{\mathcal{P}}}^{2,mo}\bar{\mathbf{e}}^{2,o}=0. \tag{15}$$

As stated before, our goal is to derive a DSA operator for the entire volume $\mathcal{V}$ without introducing unknowns on inner material interfaces $\mathcal{S}_m$. To this end, we eliminate dependencies on $\bar{\mathbf{e}}^m$ by first rewriting (15) as:

$$\bar{\mathbf{e}}^m=-\bar{\bar{\mathcal{A}}}^{-1}\cdot(\bar{\bar{\mathcal{P}}}^{1,mo}\bar{\mathbf{e}}^{1,o}+\bar{\bar{\mathcal{P}}}^{2,mo}\bar{\mathbf{e}}^{2,o}), \tag{16}$$

where $\bar{\bar{\mathcal{A}}}=(\bar{\bar{\mathcal{P}}}^{1,mm}+\bar{\bar{\mathcal{P}}}^{2,mm})$. Note that (16) expresses $\bar{\mathbf{e}}^m$ as a weighted sum of $\bar{\mathbf{e}}^{1,o}$ and $\bar{\mathbf{e}}^{2,o}$, i.e., owing to the specific choice of EDBFs, the expansion coefficients of the tangential electric field on the common surface $\mathcal{S}_m$ are readily expressed in terms of the expansion coefficients of the tangential electric field on the other surfaces $\mathcal{S}_o^1$ and $\mathcal{S}_o^2$ of $\mathcal{V}_1$ and $\mathcal{V}_2$ respectively. Second, introducing (16) into the top rows of (12) and (13) and collecting the results yields:

$$\begin{aligned}\begin{bmatrix}\bar{\mathbf{h}}^{1,o}\\ \bar{\mathbf{h}}^{2,o}\end{bmatrix} &= \begin{bmatrix}\bar{\bar{\mathcal{P}}}_{11} & \bar{\bar{\mathcal{P}}}_{12}\\ \bar{\bar{\mathcal{P}}}_{21} & \bar{\bar{\mathcal{P}}}_{22}\end{bmatrix}\cdot\begin{bmatrix}\bar{\mathbf{e}}^{1,o}\\ \bar{\mathbf{e}}^{2,o}\end{bmatrix}\\ &= \bar{\bar{\mathcal{P}}}_{tot}\cdot\begin{bmatrix}\bar{\mathbf{e}}^{1,o}\\ \bar{\mathbf{e}}^{2,o}\end{bmatrix},\end{aligned} \tag{17}$$

with

$$\bar{\bar{\mathcal{P}}}_{11}=\bar{\bar{\mathcal{P}}}^{1,oo}-\bar{\bar{\mathcal{P}}}^{1,om}\bar{\bar{\mathcal{A}}}^{-1}\bar{\bar{\mathcal{P}}}^{1,mo} \tag{18}$$

$$\bar{\bar{\mathcal{P}}}_{12}=-\bar{\bar{\mathcal{P}}}^{1,om}\bar{\bar{\mathcal{A}}}^{-1}\bar{\bar{\mathcal{P}}}^{2,mo} \tag{19}$$

$$\bar{\bar{\mathcal{P}}}_{21}=-\bar{\bar{\mathcal{P}}}^{2,om}\bar{\bar{\mathcal{A}}}^{-1}\bar{\bar{\mathcal{P}}}^{1,mo} \tag{20}$$

$$\bar{\bar{\mathcal{P}}}_{22}=\bar{\bar{\mathcal{P}}}^{2,oo}-\bar{\bar{\mathcal{P}}}^{2,om}\bar{\bar{\mathcal{A}}}^{-1}\bar{\bar{\mathcal{P}}}^{2,mo}. \tag{21}$$

The PS matrix $\bar{\bar{\mathcal{P}}}_{tot}$ is subdivided in four blocks $\bar{\bar{\mathcal{P}}}_{ij}$ $(i,j=1,2)$, mapping the electric field expansion coefficients pertaining to $\mathcal{S}_o^j$ and collected in $\bar{\mathbf{e}}^{j,o}$ onto the the rotated magnetic field expansion coefficients pertaining to $\mathcal{S}_o^i$ and collected in $\bar{\mathbf{h}}^{i,o}$. $\bar{\bar{\mathcal{P}}}_{tot}$ is thus the sought-after PS matrix of the original, piecewise homogeneously filled, volume $\mathcal{V}$.

Following a completely analogous procedure for the equivalent situation, where all materials inside $\mathcal{V}$ are replaced with the background medium, results in the PS matrix $\bar{\bar{\mathcal{P}}}_{0,tot}$. The new DSA operator, discretized using EDBFs, for $\mathcal{V}$ is now found as:

$$\bar{\bar{\mathcal{Y}}}_{tot}=\bar{\bar{\mathcal{P}}}_{tot}-\bar{\bar{\mathcal{P}}}_{0,tot}, \tag{22}$$

which contains all the information required to determine the expansion coefficients of the surface current density $\bar{\mathbf{j}}_s$ on $\mathcal{S}=\mathcal{S}_o^1\cup\mathcal{S}_o^2$ while accounting for the piecewise homogeneous character of $\mathcal{V}$ and without the need to explicitly introduce a surface current density on the material interface $\mathcal{S}_m$.

III. DSA Operator for Piecewise Homogeneous Rectilinear Polyhedra

Building upon the novel formulation of the previous section, we now enhance it to deal with general piecewise homogeneous, rectilinear polyhedra, of which an example is provided in Fig. 4. The procedure of Section II relies on the mutual orthogonality between the EDBFs on the interface surface $\mathcal{S}_m=\mathcal{S}_m^1=\mathcal{S}_m^2$. However, for an arbitrary, piecewise homogeneous, rectilinear polyhedron, this is not generally valid since $\mathcal{S}_m^1=\mathcal{S}_c$ and $\mathcal{S}_m^2=\mathcal{S}_c\cup\mathcal{S}_d$ may have different dimensions, as is the case in Fig. 4. This results in EDBFs that have different function domains and are not mutually orthogonal. Therefore, in this section, we propose a procedure that leverages suitable basis transforms to construct the DSA operator for the entire volume $\mathcal{V}$.

Consider the two rectangles presented in Fig. 5, representing $\mathcal{S}_m^1$ and $\mathcal{S}_m^2$. The original sets of EDBFs oriented in the z-direction are defined according to (6):

$$\begin{aligned}\mathcal{S}_m^1:\mathbf{f}_{n_1,p_1}(y,z) &= \sin\left(\lambda_{y_1}(y-y_0)\right)\\ &\quad\cdot\cos\left(\lambda_{z_1}(z-z_0)\right)\hat{\mathbf{z}}\end{aligned} \tag{23}$$

$$\mathcal{S}_m^2:\mathbf{g}_{n_2,p_2}(y,z)=\sin\left(\lambda_{y_2}y\right)\cos\left(\lambda_{z_2}z\right)\hat{\mathbf{z}}, \tag{24}$$

with $\lambda_{y_1}=n_1\pi/l_{y_1}$, $\lambda_{z1}=p_1\pi/l_{z_1}$ and similar expressions for λ_{y_2} and λ_{z_2}. The expressions for the y-oriented EDBFs on these surfaces have an analogous form and will not be discussed separately. We denote the area where $\mathcal{S}_m^1$ and $\mathcal{S}_m^2$ overlap $\mathcal{S}_c=\mathcal{S}_m^1\cap\mathcal{S}_m^2=\mathcal{S}_m^1$, i.e., the material interface, and the difference is denoted $\mathcal{S}_d=\mathcal{S}_m^2\backslash\mathcal{S}_m^1$. To construct a set of mutually orthogonal EDBFs on the material interface $\mathcal{S}_c$, we

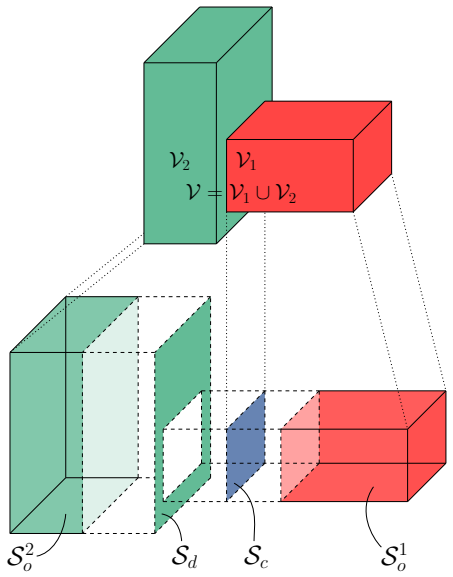

Fig. 4. Example of a piecewise homogeneous, rectilinear polyhedron $\mathcal{V}$ consisting of two homogeneous volumes $\mathcal{V}_1$ and $\mathcal{V}_2$ with wavenumbers k_1 and k_2 respectively. The surface of $\mathcal{V}_1$ is called $\mathcal{S}^1 = \mathcal{S}_o^1 \cup \mathcal{S}_c$; the surface of $\mathcal{V}_2$ is $\mathcal{S}^2 = \mathcal{S}_o^2 \cup \mathcal{S}_d \cup \mathcal{S}_c$. The total polyhedron $\mathcal{V}$ has a boundary surface $\mathcal{S} = \mathcal{S}_o^1 \cup \mathcal{S}_o^2 \cup \mathcal{S}_d$.

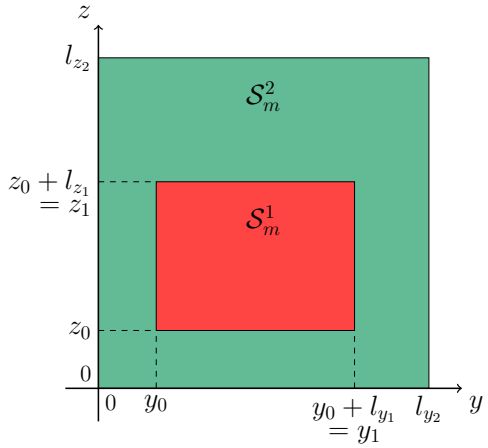

Fig. 5. Two-dimensional cross-section of the material interface for the example provided in Fig. 4. $\mathcal{S}_m^1 = \mathcal{S}_c$ and $\mathcal{S}_m^2 = \mathcal{S}_c \cup \mathcal{S}_d$ are the faces of $\mathcal{V}_1$ and $\mathcal{V}_2$, respectively, on which the material interface $\mathcal{S}_c$ is located. The dimensions of $\mathcal{S}_m^1$ and $\mathcal{S}_m^2$ are $\{l_{y_1}, l_{z_1}\}$ and $\{l_{y_2}, l_{z_2}\}$. The point (y_0, z_0) represents the origin of $\mathcal{S}_m^1$ expressed in the coordinate system of $\mathcal{S}_m^2$.

replace the original set of EDBFs (24) on $\mathcal{S}_m^2$ by two new sets. The first set is equal to (23) on $\mathcal{S}_c$ and zero on $\mathcal{S}_d$:

$$\mathbf{g}^c_{n_2',p_2'}(y,z) = \begin{cases} \mathbf{f}_{n_2',p_2'}(y,z), & \text{if } (y,z) \in \mathcal{S}_c \\ \mathbf{0} \quad , & \text{if } (y,z) \in \mathcal{S}_d \end{cases} \tag{25}$$
$$= \sum_{n_2 p_2} d_{n_2'' p_2'' n_2 p_2} \mathbf{g}_{n_2,p_2}(y,z).$$

The second set is equal to (24) on $\mathcal{S}_d$ and zero on $\mathcal{S}_c$:

$$\mathbf{g}^d_{n_2'',p_2''}(y,z) = \begin{cases} \mathbf{0} \quad , & \text{if } (y,z) \in \mathcal{S}_c \\ \sin(\frac{n_2''\pi}{l_{y_2}} y) \cos(\frac{p_2''\pi}{l_{z_2}} z)\hat{\mathbf{z}}, & \text{if } (y,z) \in \mathcal{S}_d \end{cases} \tag{26}$$
$$= \sum_{n_2 p_2} d_{n_2'' p_2'' n_2 p_2} \mathbf{g}_{n_2,p_2}(y,z).$$

As indicated, both sets may be derived from the original set (24) by applying an appropriate basis transformation. The corresponding coefficients, $c_{n_2' p_2' n_2 p_2}$ and $d_{n_2'' p_2'' n_2 p_2}$, are determined by computing the pertinent inner products. These inner products for the two faces presented in Fig. 5 are given by:

$$c_{n_2' p_2' n_2 p_2} = \langle \mathbf{g}^c_{n_2',p_2'}, \mathbf{g}_{n_2,p_2} \rangle_c = \frac{\iint_{\mathcal{S}_c} \mathbf{g}^c_{n_2',p_2'}(y,z) \cdot \mathbf{g}_{n_2,p_2}(y,z)\, dy\, dz}{\iint_{\mathcal{S}_m^2} \mathbf{g}_{n_2,p_2}(y,z) \cdot \mathbf{g}_{n_2,p_2}(y,z)\, dy\, dz}, \tag{27}$$

$$d_{n_2'' p_2'' n_2 p_2} = \langle \mathbf{g}^d_{n_2'',p_2''}, \mathbf{g}_{n_2,p_2} \rangle_d = \frac{\iint_{\mathcal{S}_d} \mathbf{g}^d_{n_2'',p_2''}(y,z) \cdot \mathbf{g}_{n_2,p_2}(y,z)\, dy\, dz}{\iint_{\mathcal{S}_m^2} \mathbf{g}_{n_2,p_2}(y,z) \cdot \mathbf{g}_{n_2,p_2}(y,z)\, dy\, dz}, \tag{28}$$

where the denominator is a normalization constant to ensure that $c_{n_2' p_2' n_2 p_2} = \delta_{n_2,n_2'} \delta_{p_2,p_2'}$ and $d_{n_2'' p_2'' n_2 p_2} = \delta_{n_2,n_2''} \delta_{p_2,p_2''}$ in the limiting case of $\mathcal{S}_c = \mathcal{S}_m^1 = \mathcal{S}_m^2$. Owing to the trigonometric forms, analytical expressions are found for (27) and (28), and provided in Appendix A. Similar expressions for the other faces, with other orientations, are also readily found.

Using the analytical forms of (27) and (28), we can now readily construct transformation matrices $\bar{\bar{C}}$ and $\bar{\bar{D}}$ collecting these coefficients, so that:

$$\bar{\mathbf{e}}^{2,m} = \bar{\bar{C}} \cdot \bar{\mathbf{e}}_c^{2,m} + \bar{\bar{D}} \cdot \bar{\mathbf{e}}_d^{2,m} \tag{29}$$
$$\bar{\mathbf{h}}^{2,m} = \bar{\bar{C}} \cdot \bar{\mathbf{h}}_c^{2,m} + \bar{\bar{D}} \cdot \bar{\mathbf{h}}_d^{2,m}, \tag{30}$$

where:

- the vectors $\bar{\mathbf{e}}^{2,m}$ and $\bar{\mathbf{h}}^{2,m}$ contain the expansion coefficients of the tangential electric field and rotated tangential magnetic field on $\mathcal{S}_m$ corresponding to the original set of EDBFs (24), as before;
- the vectors $\bar{\mathbf{e}}_c^{2,m}$ and $\bar{\mathbf{h}}_c^{2,m}$ contain the expansion coefficients of the tangential electric field and rotated tangential magnetic field on $\mathcal{S}_c$ corresponding to the set of basis functions (25);
- and the vectors $\bar{\mathbf{e}}_d^{2,m}$ and $\bar{\mathbf{h}}_d^{2,m}$ contain the expansion coefficients of the tangential electric field and rotated tangential magnetic field on $\mathcal{S}_d$ corresponding to the set of basis functions (26),

respectively.

Subsequently, using a similar methodology as described in Section II, we impose continuity of the tangential magnetic field on $\mathcal{S}_c$:

$$\begin{aligned}\bar{\mathbf{h}}^{1,m} + \bar{\bar{C}}^T \bar{\mathbf{h}}^{2,m} &= \bar{\bar{\mathcal{P}}}^{1,mm}\bar{\mathbf{e}}^{1,m} + \bar{\bar{\mathcal{P}}}^{1,mo}\bar{\mathbf{e}}^{1,o} \\ &\quad + \bar{\bar{C}}^T\bar{\bar{\mathcal{P}}}^{2,mm}\bar{\bar{C}}\,\bar{\mathbf{e}}_c^{2,m} + \bar{\bar{C}}^T\bar{\bar{\mathcal{P}}}^{2,mm}\bar{\bar{D}}\,\bar{\mathbf{e}}_d^{2,m} \\ &\quad + \bar{\bar{C}}^T\bar{\bar{\mathcal{P}}}^{2,mo}\bar{\mathbf{e}}^{2,o} \\ &= 0. \end{aligned} \tag{31}$$

Assuming that, after performing the basis transformation, $\mathcal{V}_1$ and $\mathcal{V}_2$ have the same number of EDBFs on the interface $\mathcal{S}_c$ and imposing continuity of the tangential electric field on $\mathcal{S}_c$, i.e., $\bar{\mathbf{e}}^m = \bar{\mathbf{e}}^{1,m} = \bar{\mathbf{e}}_c^{2,m}$, results in:

$$\begin{aligned}\bar{\mathbf{e}}^m = &-\bar{\bar{\mathcal{A}}}'^{-1}\cdot \\ &(\bar{\bar{\mathcal{P}}}^{1,mo}\bar{\mathbf{e}}^{1,o} + \bar{\bar{C}}^T\bar{\bar{\mathcal{P}}}^{2,mo}\bar{\mathbf{e}}^{2,o} + \bar{\bar{C}}^T\bar{\bar{\mathcal{P}}}^{2,mm}\bar{\bar{D}}\,\bar{\mathbf{e}}_d^{2,m}),\end{aligned} \tag{32}$$

where $\bar{\bar{\mathcal{A}}}' = (\bar{\bar{\mathcal{P}}}^{1,mm} + \bar{\bar{C}}^T\bar{\bar{\mathcal{P}}}^{2,mm}\bar{\bar{C}})$. Equation (32) expresses $\bar{\mathbf{e}}^m = \bar{\mathbf{e}}^{1,m} = \bar{\mathbf{e}}_c^{2,m}$ as a weighted sum of $\bar{\mathbf{e}}^{1,o}$, $\bar{\mathbf{e}}^{2,o}$ and $\bar{\mathbf{e}}_d^{2,m}$, i.e., the expansion coefficients of the tangential electric field on the common surface $\mathcal{S}_c$ are expressed in terms of the expansion coefficients of the tangential electric field on the other surfaces $\mathcal{S}_o^1$, $\mathcal{S}_o^2$ and $\mathcal{S}_d$. Just as in Section II, by leveraging (32), the dependence of the expansion coefficients for the rotated tangential magnetic field at $\mathcal{S}$ on the expansion coefficients for the tangential electric field at the interface $\mathcal{S}_c$ is eliminated, resulting in the following structure for the PS operator of the total volume $\mathcal{V}$:

$$\begin{aligned}\begin{bmatrix}\bar{\mathbf{h}}^{1,o}\\ \bar{\mathbf{h}}^{2,o}\\ \bar{\mathbf{h}}_d^{2,m}\end{bmatrix} &= \begin{bmatrix}\bar{\bar{\mathcal{P}}}_{11} & \bar{\bar{\mathcal{P}}}_{12} & \bar{\bar{\mathcal{P}}}_{13}\\ \bar{\bar{\mathcal{P}}}_{21} & \bar{\bar{\mathcal{P}}}_{22} & \bar{\bar{\mathcal{P}}}_{23}\\ \bar{\bar{\mathcal{P}}}_{31} & \bar{\bar{\mathcal{P}}}_{32} & \bar{\bar{\mathcal{P}}}_{33}\end{bmatrix}\cdot\begin{bmatrix}\bar{\mathbf{e}}^{1,o}\\ \bar{\mathbf{e}}^{2,o}\\ \bar{\mathbf{e}}_d^{2,m}\end{bmatrix} \\ &= \bar{\bar{\mathcal{P}}}_{tot}\cdot\begin{bmatrix}\bar{\mathbf{e}}^{1,o}\\ \bar{\mathbf{e}}^{2,o}\\ \bar{\mathbf{e}}_d^{2,m}\end{bmatrix},\end{aligned} \tag{33}$$

with

$$\bar{\bar{\mathcal{P}}}_{11} = \bar{\bar{\mathcal{P}}}^{1,oo} - \bar{\bar{\mathcal{P}}}^{1,om}\bar{\bar{\mathcal{A}}}'^{-1}\bar{\bar{\mathcal{P}}}^{1,mo} \tag{34}$$

$$\bar{\bar{\mathcal{P}}}_{12} = -\bar{\bar{\mathcal{P}}}^{1,om}\bar{\bar{\mathcal{A}}}'^{-1}\bar{\bar{C}}^T\bar{\bar{\mathcal{P}}}^{2,mo} \tag{35}$$

$$\bar{\bar{\mathcal{P}}}_{13} = -\bar{\bar{\mathcal{P}}}^{1,om}\bar{\bar{\mathcal{A}}}'^{-1}\bar{\bar{C}}^T\bar{\bar{\mathcal{P}}}^{2,mm}\bar{\bar{D}} \tag{36}$$

$$\bar{\bar{\mathcal{P}}}_{21} = -\bar{\bar{\mathcal{P}}}^{2,om}\bar{\bar{C}}\bar{\bar{\mathcal{A}}}'^{-1}\bar{\bar{\mathcal{P}}}^{1,mo} \tag{37}$$

$$\bar{\bar{\mathcal{P}}}_{22} = \bar{\bar{\mathcal{P}}}^{2,oo} - \bar{\bar{\mathcal{P}}}^{2,om}\bar{\bar{C}}\bar{\bar{\mathcal{A}}}'^{-1}\bar{\bar{C}}^T\bar{\bar{\mathcal{P}}}^{2,mo} \tag{38}$$

$$\bar{\bar{\mathcal{P}}}_{23} = \bar{\bar{\mathcal{P}}}^{2,om}\bar{\bar{D}} - \bar{\bar{\mathcal{P}}}^{2,om}\bar{\bar{C}}\bar{\bar{\mathcal{A}}}'^{-1}\bar{\bar{C}}^T\bar{\bar{\mathcal{P}}}^{2,mm}\bar{\bar{D}} \tag{39}$$

$$\bar{\bar{\mathcal{P}}}_{31} = -\bar{\bar{D}}^T\bar{\bar{\mathcal{P}}}^{2,mm}\bar{\bar{C}}\bar{\bar{\mathcal{A}}}'^{-1}\bar{\bar{\mathcal{P}}}^{1,mo} \tag{40}$$

$$\bar{\bar{\mathcal{P}}}_{32} = \bar{\bar{D}}^T\bar{\bar{\mathcal{P}}}^{2,mo} - \bar{\bar{D}}^T\bar{\bar{\mathcal{P}}}^{2,mm}\bar{\bar{C}}\bar{\bar{\mathcal{A}}}'^{-1}\bar{\bar{C}}^T\bar{\bar{\mathcal{P}}}^{2,mo} \tag{41}$$

$$\bar{\bar{\mathcal{P}}}_{33} = \bar{\bar{D}}^T\bar{\bar{\mathcal{P}}}^{2,mm}\bar{\bar{D}} - \bar{\bar{D}}^T\bar{\bar{\mathcal{P}}}^{2,mm}\bar{\bar{C}}\bar{\bar{\mathcal{A}}}'^{-1}\bar{\bar{C}}^T\bar{\bar{\mathcal{P}}}^{2,mm}\bar{\bar{D}}. \tag{42}$$

Note that in the limiting case of $\mathcal{S}_c = \mathcal{S}_1^m = \mathcal{S}_2^m$, (33) reduces to (17) since in this case $\bar{\bar{C}} = \bar{\bar{I}}$ and $\bar{\bar{D}} = \bar{\bar{0}}$. $\bar{\bar{\mathcal{P}}}_{tot}$ is the PS matrix of $\mathcal{V}$ for the original situation presented in Fig. 4. Using the same methodology but replacing the volume's media with the background medium, yields the PS operator $\bar{\bar{\mathcal{P}}}_{0,tot}$ for the equivalent situation. Combining $\bar{\bar{\mathcal{P}}}_{tot}$ and $\bar{\bar{\mathcal{P}}}_{0,tot}$ allows to construct the DSA operator $\bar{\bar{\mathcal{Y}}}_{tot} = \bar{\bar{\mathcal{P}}}_{tot} - \bar{\bar{\mathcal{P}}}_{0,tot}$ for the rectilinear polyhedron $\mathcal{V}$. Moreover, all matrix elements involved in the construction of this new DSA operator are available in closed-form, analytical expressions, enhancing its accuracy and efficiency.

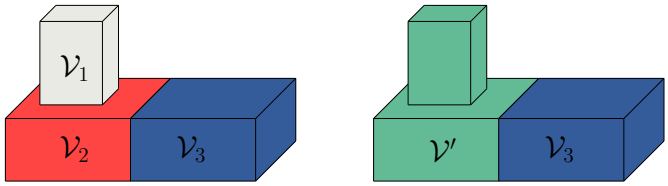

Fig. 6. Example of a piecewise homogeneous, rectilinear polyhedron with multiple material interfaces.

IV. Extension to Arbitrary Piecewise Homogeneous Volumes.

A. Multiple Material Interfaces

So far, our discussion focused on removing a single rectangular material interface within a given volume $\mathcal{V}$. Nevertheless, the proposed method is readily extended to multiple material interfaces. Consider the situation presented in Fig. 6a, where the volume $\mathcal{V} = \mathcal{V}_1 \cup \mathcal{V}_2 \cup \mathcal{V}_3$ contains two material interfaces. In a first step, only the volume $\mathcal{V}' = \mathcal{V}_1 \cup \mathcal{V}_2$ is considered. The relevant material interface is removed using the procedure described in Section III. The resulting situation is provided in Fig. 6b. The second step considers the total volume $\mathcal{V} = \mathcal{V}' \cup \mathcal{V}_3$ with now only a single material interface, which is readily removed employing the method described in Section II.

Alternatively, both interfaces are eliminated simultaneously, rather than handling them sequentially, by enforcing continuity of the tangential electric field and tangential magnetic field concurrently for both interfaces. This approach necessitates only a single execution of the presented method, albeit at the expense of an increased matrix size during computation. Consequently, selecting the sequential or direct method involves a trade-off between computation time and memory usage: the sequential method takes longer but consumes less memory, while the direct method is faster but more memory-intensive. This trade-off will be illustrated in the numerical examples.

B. Arbitrary Shaped Volumes

While the derivations presented in Sections II and III assume rectilinear interfaces, its core principles are not inherently restricted to such geometries. The essential requirement is that the PS operators for each homogeneous subvolume be representable in terms of EDBFs, which is feasible for canonical shapes, e.g., spheres and cylinders, but also for arbitrary smoothly varying shapes through, e.g., spline-based representations [30].

A key feature of our 3-D DSA operator construction is the use of analytical expressions for the PS matrix elements, which

are derived from the eigenmodes of the individual subvolumes. While these are readily available for canonical geometries, computing them for arbitrary smooth volumes is non-trivial and/or computationally expensive. However, prior work [21], [31] in 2-D has shown that DSA operators can be constructed for arbitrary polygons without relying on eigenmodes. A similar extension to 3-D, combined with our proposed method, would enable the modeling of arbitrarily shaped, piecewise homogeneous volumes, significantly broadening the applicability of our approach. This is presently under investigation.

V. Solution of the Outside Problem

Using the previously derived DSA operators, the original problem is reformulated by replacing all materials with the background medium, i.e., free space in our examples, while introducing appropriate fictitious differential surface currents on the outer surfaces of the object. This reformulated problem, now defined entirely in the background medium, can be solved using the EFIE. The EFIE, formulated under the assumption of vanishing magnetic surface currents as expressed in (28) of [32], is discretized via the Method of Moments (MoM), employing rooftop basis functions that naturally conform to the rectangular surface grid of the considered rectilinear objects. However, the DSA operators $\bar{\bar{\mathcal{Y}}}_{tot}$ derived in the previous sections are still expressed in terms of EDBFs. To proceed with the MoM formulation, we project $\bar{\bar{\mathcal{Y}}}_{tot}$ onto rooftop basis functions, yielding $\bar{\bar{Y}}_{roof}$. A detailed explanation of this procedure is provided in [26]. Note that, as is typical for all single-source boundary element methods, the DSA operator $\bar{\bar{Y}}_{\text{roof}}$ exhibits a dense matrix structure. Combining the EFIE with the DSA operator, now both discretized using rooftop functions, results in the following linear system:

$$(\bar{\bar{G}} + \bar{\bar{Y}}_{roof} \cdot \bar{\bar{G}}^{-1} \cdot \bar{\bar{Z}}) \cdot \bar{\mathbf{J}} = \bar{\bar{Y}}_{roof} \cdot \bar{\bar{G}}^{-1} \cdot \bar{\mathbf{E}}, \tag{43}$$

with

$$\bar{\bar{G}}_{ij} = \int_{\mathcal{S}} \mathbf{t}_i(\mathbf{r}) \cdot \mathbf{t}_j(\mathbf{r}') dS \tag{44}$$

$$\bar{\mathbf{E}}_i = \int_{\mathcal{S}_i} \mathbf{t}_i(\mathbf{r}) \cdot \mathbf{e}^t_{inc}(\mathbf{r}) dS \tag{45}$$

$$\bar{\bar{Z}}_{ij} = j\omega\mu_0 \int_{\mathcal{S}_i} \int_{\mathcal{S}_j} G(\mathbf{r},\mathbf{r}') \mathbf{t}_i(\mathbf{r}) \cdot \mathbf{t}_j(\mathbf{r}') dS' dS + \frac{1}{j\omega\epsilon_0} \int_{\mathcal{S}_i} \int_{\mathcal{S}_j} G(\mathbf{r},\mathbf{r}') \nabla \cdot \mathbf{t}_i(\mathbf{r}) \nabla' \cdot \mathbf{t}_j(\mathbf{r}') dS' dS \tag{46}$$

$$G(\mathbf{r},\mathbf{r}') = \frac{e^{-jk_0|\mathbf{r}-\mathbf{r}'|}}{4\pi|\mathbf{r}-\mathbf{r}'|}, \tag{47}$$

where $\mathbf{e}^t_{inc}(\mathbf{r})$ is the tangential electric field that is incident on the considered object and $\mathbf{t}_i(\mathbf{r})$ is the rooftop basis function, defined according to [26]. Note that, in our formulation, the Gramian matrix $\bar{\bar{G}}$ of the rooftop basis is block-diagonal with small, sparse blocks, enabling efficient computation of its inverse without introducing a significant computational burden, even for large-scale problems. Solving (43), yields the sought-after fictitious surface current densities $\bar{\mathbf{J}}$, which fully characterize the electromagnetic problem. To facilitate the computation of broadband impedance responses, the EFIE formulation presented in (43) is reformulated using the augmented EFIE approach [33].

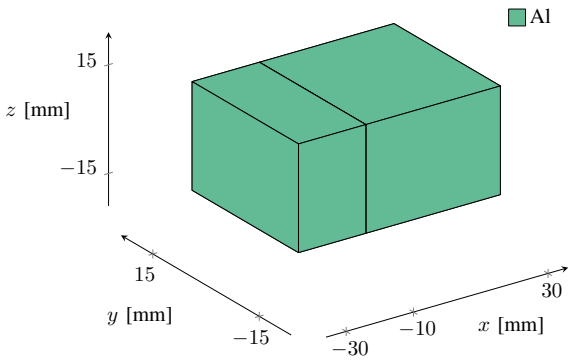

Fig. 7. Aluminum block ($\sigma = 3.77 \times 10^7$ S/m) with dimensions 60 mm × 30 mm × 30 mm. An artificial material interface is introduced at $x = -10$ mm, dividing the block into two smaller blocks with dimensions 20 mm × 30 mm × 30 mm and 40 mm × 30 mm × 30 mm.

VI. Numerical Results

A. Validation Examples

The first validation example considers a monolithic aluminum block ($\sigma = 3.77 \times 10^7$ S/m) with dimensions 60 mm × 30 mm × 30 mm. We introduce an artificial material interface in this block, as depicted in Fig. 7, to verify the accuracy of the newly proposed $\mathcal{Y}$-operator in the limiting case of a fully homogeneous cuboid. The reference solution is obtained by modeling the entire block without artificial interface and adopting the method proposed in [26]. (Note thas this method [26] has already been thoroughly validated through comparison with academic and commercial solvers.) Possible coarse mesh effects are mitigated by setting the total number of rooftops at 864. The number of employed entire domain basis functions is set at {12,12,12} in the x-, y- and z-direction, respectively, for each individual block in Fig. 7. For the reference solution [26], which considers the entire block, the number of EDBFs is set at {20,15,15}.

A plane wave, propagating in the positive y-direction with its electric field polarized along the vector $\bar{\mathbf{p}} = (1, 0, 1)$ at a frequency of 3.5 GHz, is incident on the aluminum block of Fig. 7. The resulting bistatic radar cross-section (RCS) in the xy-plane, as a function of the azimuth angle ϕ, is provided in Fig. 8. Additionally, the scattered electric field, on a circle in the xy-plane with radius of one wavelength, i.e., 8.57 cm, and centered about the origin, is observed. Fig. 9 provides the magnitude and phase of the scattered electric field. For both the RCS and the scattered electric field, a perfect agreement is observed between the method described in this work and the reference solution [26]. This demonstrates that the newly proposed approach, designed for piecewise homogeneous volumes, retains its accuracy in the limiting case of a fully homogeneous object.

We would like to clarify here that, for all our numerical examples, the amount of EDBFs was chosen to be sufficiently

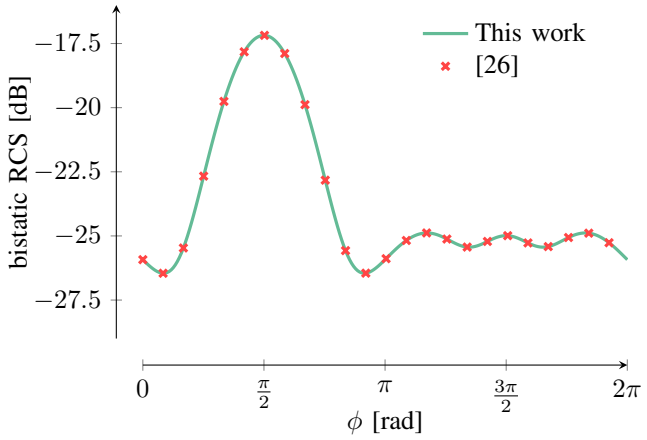

Fig. 8. Bistatic radar cross-section in the xy-plane for a plane wave incident on the aluminum block presented in Fig. 7. The plane wave is propagating in the positive y-direction with the electric field polarized along $\bar{\mathbf{p}} = (1, 0, 1)$ at a frequency of 3.5 GHz.

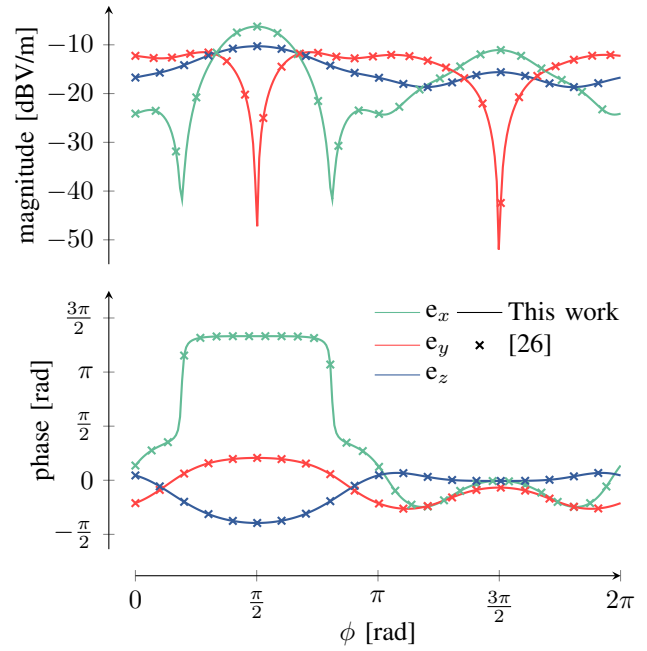

Fig. 9. Magnitude and phase of the scattered electric field, on a circle in the xy-plane with radius of one wavelength and centered about the origin, for a plane wave incident on the aluminum block presented in Fig. 7. The plane wave is propagating in the positive y-direction with the electric field polarized along $\bar{\mathbf{p}} = (1, 0, 1)$ at a frequency of 3.5 GHz.

large to ensure accurate and reliable results. To illustrate this, we set the number of EDBFs to $\{N, N, N\}$ for the example of Fig. 7 and compute the relative error of e_x, averaged across ϕ, with respect to the results obtained using [26]. The resulting plot Fig. 10 demonstrates that the error systematically decreases with increasing amount of EDBFs. In this work, a relative error of 10^{-6} was deemed adequate, and the chosen number of EDBFs was selected to provide a safe margin below this threshold, balancing accuracy with computational efficiency. A general criterion or heuristic for selecting the minimal effective number of EDBFs based on the desired accuracy has yet to be established.

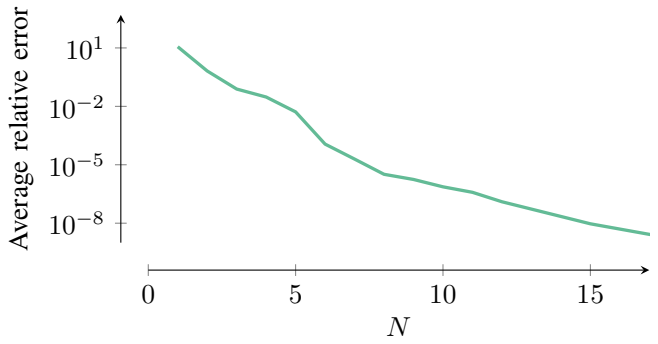

Fig. 10. Relative error of e_x, averaged over ϕ, between the proposed method with $\{N, N, N\}$ EDBFs and the reference results obtained using the method from [26].

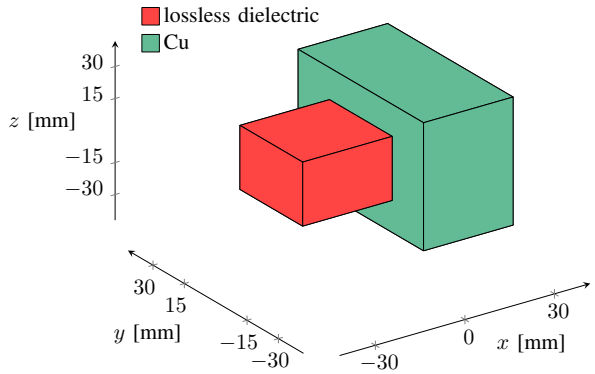

Fig. 11. Polyhedron consisting of two different materials. The large block with dimensions 30 mm × 60 mm × 60 mm is copper ($\sigma = 5.8 \times 10^7$ S/m). The smaller block with dimensions 30 mm × 30 mm × 30 mm is a dielectric ($\epsilon_r = 4.0$).

For the second validation example, we shift our attention towards an actual piecewise homogeneous object with significant material contrast. Consider the object presented in Fig. 11: a piecewise homogeneous polyhedron composed of two distinct materials. The two materials constituting the polyhedron are copper ($\sigma = 5.8 \times 10^7$ S/m) and a dielectric ($\epsilon_r = 4.0$). For this example, the mesh of our proposed method consists of 640 edges (and, thus, rooftop functions); the number of EDBFs is set at $\{10,10,10\}$ in the x-, y-, and z-direction, respectively, for the dielectric block, and $\{12,15,15\}$ for the copper block. Our new method is compared with the wire approach of [26], using the same number of EDBFs as our method, as well as with CST Microwave Studio's (CST MWS) frequency-domain solver, a commercial solver based on the finite-element method [34].

A plane wave propagating in the positive x-direction with a y-polarized electric field at a frequency of 2 GHz, is incident on the object of Fig. 11. The resulting bistatic radar cross-section in the xy-plane, as a function of the azimuth angle ϕ, is depicted in Fig. 12. An excellent agreement is observed between our proposed method and CST MWS, with only slight deviations at specific angles due to the vanishingly small scattered power levels. Furthermore, the solution obtained with the wire method of [26] deviates significantly from the two

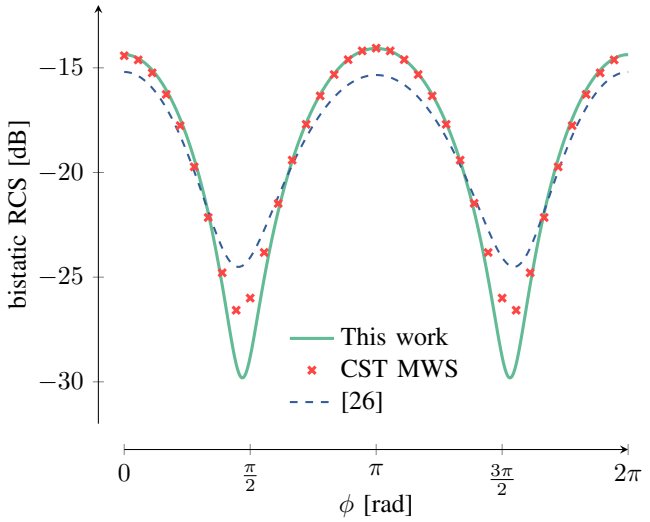

Fig. 12. Bistatic radar cross-section in the xy-plane for a plane wave incident on the object presented in Fig. 11. The plane wave is propagating in the positive x-direction with a y-polarized electric field at a frequency of 2 GHz.

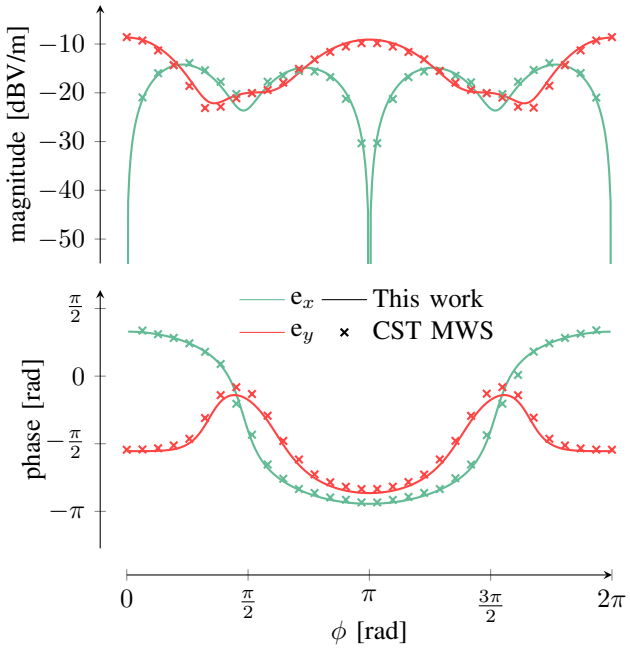

Fig. 13. Magnitude and phase of the scattered electric field, on a circle in the xy-plane with radius of one wavelength, for a plane wave incident on the object presented in Fig. 11. The plane wave is propagating in the positive x-direction with a y-polarized electric field at a frequency of 2 GHz.

other solutions, clearly showing — as expected — that this approach loses accuracy in the presence of non-conducting materials. This shortcoming of the wire method underscores the need for our novel approach to maintain precision and validity. Additionally, for the same incoming plane wave, the scattered electric field at a distance of one wavelength, i.e., 14.99 cm, is observed in the xy-plane as function of ϕ. Both the magnitude and phase of the x- and y-component of the electric field are provided in Fig. 13; the z-component is not presented as its values are numerically zero due to the polarization of the plane wave. For conciseness and readability, only the CST MWS reference result is included. Once again, a very good agreement is observed between our new method and CST MWS, confirming that our method is accurate even in the presence of a high contrast material interface.

To complete this section, Table I provides the peak memory usage and computation time required to obtain the presented results. The simulations for both our method and the approach proposed in [26] were conducted using a single core on a machine with a 1.8 GHz CPU and 16 GB RAM. The CST MWS solution was obtained using a single core on a machine with 2.1 GHz CPU and 64 GB of RAM. For the first validation example of Fig. 7, our method exhibits a computation time comparable to that of [26], with only a slight increase in peak memory usage. This shows that the additional computational steps in our approach introduce minimal overhead while extending its applicability to a wider range of scenarios. For the second validation example of Fig. 11, it is clear that our method requires significantly less computational resources than CST MWS. The computation time is a factor 22 lower and the memory usage is decreased by a factor 88. Moreover, our method was implemented in Python without the use of specialized acceleration techniques or efficiency-enhancing optimizations for the exterior problem described in Section V.

TABLE I
PEAK MEMORY USAGE AND COMPUTATION TIME FOR THE VALIDATION EXAMPLES PRESENTED IN FIG. 7 AND FIG. 11.

Metric	This work	CST MWS	[26]
Fig. 7			
Computation time [s]	49.0	-	48.3
Peak memory usage [MB]	136.6	-	105.8
Fig. 11			
Computation time [s]	42.2	929.0	62.5
Peak memory usage [MB]	291.5	25680.9	127.6

B. Application Examples

1) Conductor With Right-Angled Bend: A first application example is presented in Fig. 14, constituting a right-angled corner in a conductor consisting of two distinct metals, i.e., copper ($\sigma = 5.8 \times 10^7$ S/m) and tungsten ($\sigma = 1.8 \times 10^7$ S/m). To determine the impedance of the corner, a unit current $I = 1$ A is injected into the tungsten part of the corner and extracted from the copper part, as indicated on Fig. 14, and the potential difference between both terminals is measured. The total number of rooftop functions is fixed at 112. For the situation shown in Fig. 14a, the number of EDBFs in the x-, y- and z-direction is set to {12,12,12} and {12,15,12} for the tungsten and copper block, respectively. In the alternative scenario of Fig. 14b, the number of EDBFs is set to {12,12,12} for each individual block.

In a first solution, we consider the single material interface between the tungsten and copper and employ the method described in Section III to resolve the material interface.

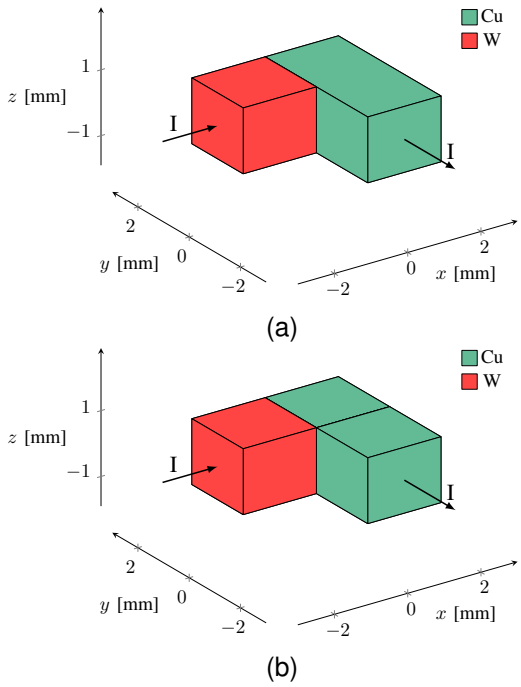

Fig. 14. Right-angled corner consisting of two distinct metals. The smallest block is made of tungsten ($\sigma = 1.8 \times 10^7$ S/m) and has dimensions 2 mm $\times$ 2 mm $\times$ 2 mm. The larger cuboid has dimensions 2 mm $\times$ 4 mm $\times$ 2 mm and is made of copper ($\sigma = 5.8 \times 10^7$ S/m). A unit current $I = 1$ A is injected into the tungsten block and extracted from the copper block, allowing to calculate the impedance of the total corner. In (a), the single material interface between the tungsten and copper is considered. In (b), a second artificial material interface is added in the copper block at $y = 0$.

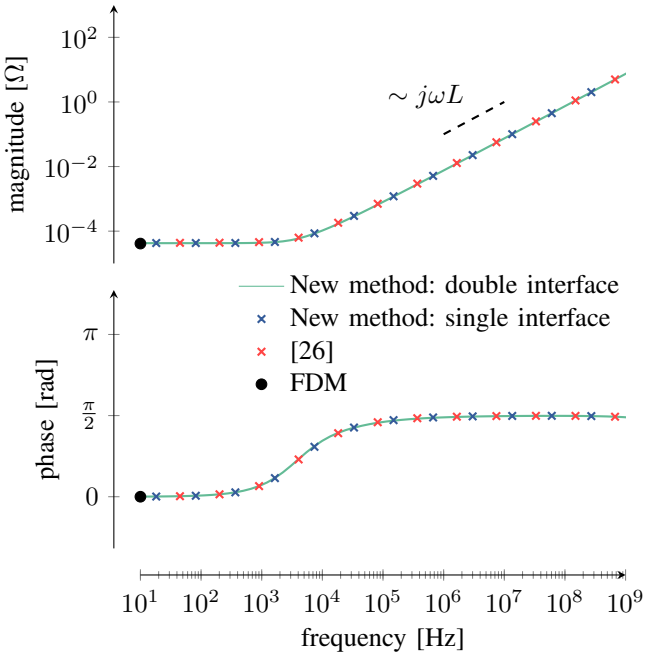

Fig. 15. Impedance response, magnitude and phase, of the right-angled bend of Fig. 14 when a unit current is injected.

A second solution consists of adding an artificial material interface in the copper block at $y = 0$ and using the method described in Section IV-A to resolve both interfaces. We added the artificial material interface in order to have aligning EDBFs for both interfaces, negating the need to perform a basis transform, but at the cost of having two material interfaces instead of one. We validate both our solutions with the wire method of [26], which still provides accurate results for this configuration consisting of good conductors only.

Fig. 15 presents the magnitude and phase of the corner's impedance from 10 Hz to 1 GHz. At 10 Hz, the impedance is dominated by the resistance since this frequency is too low for any noticeable inductive effect, given the corner's dimensions. Additionally, at this frequency, using the well-known formula for the skin depth, $\delta = \sqrt{\frac{2}{\omega\mu\sigma}}$, we find that the skin depth is of the order 20-40 mm depending on the specific conductor, indicating that the skin-effect has not yet developed at this frequency. Consequently, the low-frequency value of the impedance is verified using the DC resistance obtained from a finite difference method (FDM) solving the relevant Laplace problem. Observing the low-frequency range of Fig. 15, it is clear that both proposed methods nicely align with the FDM solution. When the frequency increases, inductive effects become more noticeable and start to dominate the total impedance, as observed for both the magnitude and phase of the bend. For sufficiently high frequencies, the magnitude has the expected slope of +20 dB/dec caused by the factor $j\omega L$ in the total impedance, where L is the inductance of the bend. Additionally, the phase approaches the expected value of $\pi/2$, confirming that the inductive effects dominate the total impedance at increasing frequencies. Both proposed solutions agree very well with the wire approach of [26] across the entire frequency range, verifying the broadband accuracy of our novel method.

As discussed in Section IV-A, the double interface problem can be addressed either sequentially or directly, depending on the available computational resources. Figure 16 presents the percentage differences in computation time and peak memory usage of the direct method relative to the sequential method. In these simulations, the number of EDBFs for each individual block was set to $\{N, N, N\}$. The results illustrate the trade-off described in Section IV-A: the direct method achieves shorter computation times but requires more memory, whereas the sequential method does the opposite. No noticeable difference in the condition number was observed between the two approaches. Both methods yield the results presented in Figure 15, and the corresponding performance data are reported in Table II.

2) Planar MIMcap: For our final application example, we study a planar metal-insulator-metal capacitor (MIMcap), an important topology adopted for on-chip capacitors in various state-of-the-art applications [35]–[37]. An example of such a capacitor is provided in Fig. 17. The capacitor plates and contacts are made of copper ($\sigma = 5.8 \times 10^7$ S/m) and the dielectric is a high-k material, with a relative permittivity $\epsilon_r = 19.3$ [38]. An adapted version of this topology is presented in Fig. 18, featuring half the number of vias connecting the contacts to the capacitor plates.

A unit current is injected into the first contact and extracted from the second contact, as shown in Fig. 17 and 18. The

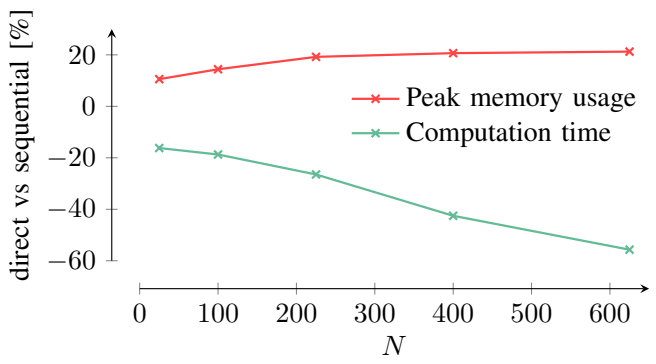

Fig. 16. Percentage differences in computation time and peak memory usage for the direct method relative to the sequential method, each using $\{N, N, N\}$ EDBFs.

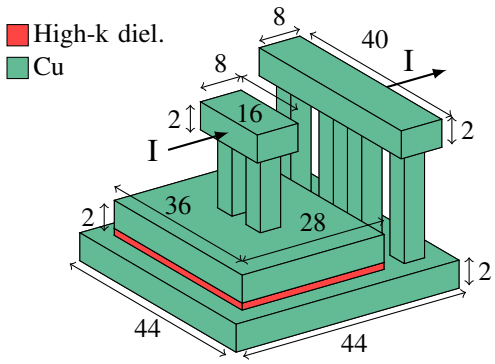

Fig. 17. Planar metal-insulator-metal capacitor (MIMcap) consisting of copper plates and contacts ($\sigma = 5.8 \times 10^7$ S/m) and a high-k dielectric ($\epsilon_r = 19.3$) with a thickness of 500 nm. All other dimensions indicated on the figure are expressed in micrometer. The plates and contacts are connected using a total of six copper vias, all having a 4 µm × 4 µm cross-section. The two vias connected to the top plate of the capacitor have a height of 5.5 µm, the other four vias have a height of 8 µm. To calculate the impedance of the MIMcap, a unit current $I = 1$ A is injected into the first contact and extracted from the second one.

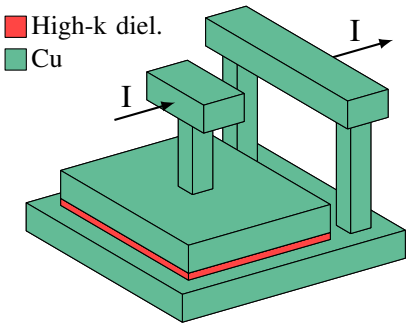

Fig. 18. Planar MIMcap similar to the one presented in Fig. 17, but the number of copper vias connecting the plates to the contacts has been reduced from six to three.

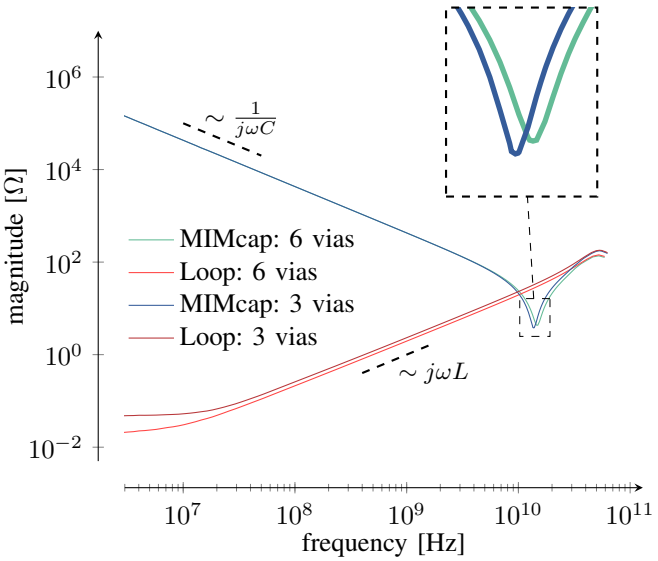

Fig. 19. Impedance response of the MIMcaps presented in Fig. 17 and 18 (blue and green line, respectively). The impedance of the shorted capacitors, i.e., the loop impedance, is also provided for both situations (red lines).

impedance of both topologies is consequently determined by taking the potential difference between both contacts. The resulting impedances, as function of frequency, are presented in Fig. 19.

For frequencies up to about 2 GHz, the capacitive behavior, governed by $1/j\omega C$, dominates the total impedance and both topologies yield the same result. This is to be expected, since changing the number of vias has negligible influence on the total capacitance of the structure. Fitting $Z = 1/j\omega C$ to our obtained results, the capacitance of the MIMcaps is determined to be 0.363 pF. We may validate this result using the analytical value obtained for a parallel-plate capacitor:

$$C_{pp} = \frac{A\epsilon_0\epsilon_r}{d}, \tag{48}$$

with area A, plate spacing d and relative dielectric constant ϵ_r. Using (48), we obtain a value of 0.344 pF which approximates the value obtained using our numerical method. The small difference is of course attributed to additional fringing capacitance since the bottom plate has a larger surface area than the dielectric and top plate, as observed in Fig. 17. At higher frequencies, the impedance response of the capacitor deviates from its ideal capacitive behavior due to the onset of self-resonance, which arises from the parasitic inductance inherent in the component's physical construction [1]. The self-resonance frequency is determined using

$$f_{SRF} = \frac{1}{2\pi\sqrt{LC}}, \tag{49}$$

where L and C are the inductance and capacitance of the structure, respectively. Using the self-resonance frequency values obtained from Fig. 19 and the previously determined value for the capacitance of the MIMcaps, an estimate can be made for the inductance of both considered MIMcaps. The estimated

TABLE II
PEAK MEMORY USAGE AND COMPUTATION TIME PER FREQUENCY POINT FOR THE RESULTS PRESENTED IN FIG. 15 AND FIG. 19.

Metric	This work	[26]
Fig. 15		
Computation time [s]	8.7 (double interface: seq.) 6.8 (double interface: dir.) 5.6 (single interface)	4.9
Peak memory usage [MB]	169.8 (double interface: seq.) 199.7 (double interface: dir.) 296.7 (single interface)	101.3
Fig. 19		
Computation time [s]	354.8	-
Peak memory usage [MB]	1716.7	-

inductances are 0.302 nH and 0.358 nH for the MIMcap with six vias and three vias, respectively. As expected, reducing the number of vias lowers the amount of parallel paths for the current resulting in an increased inductance. On Fig. 19, we also plotted the loop impedances, i.e., the impedance of the structures when the dielectric is replaced by a copper plate. These loop inductances are determined using our proposed method. Starting from around 0.1 GHz, the inductive effects, governed by the factor $j\omega L$, dominate the resistive part of the total impedance. From the slopes of the curves, the inductances are determined to be 0.302 nH and 0.358 nH for the case with six and three vias, respectively, which exactly matches our previously made estimates.

Attempts to simulate this structure using CST MWS were unsuccesful, as the solver was unable to converge to a solution due to the presence of the very thin dielectric layer sandwiched between two thicker conductors. Additionally, the high operating frequency, which results in a small skin depth, combined with the high relative permittivity of the dielectric, further contributed to the numerical instability and computational challenges. For completeness, Table II provides the computation times and peak memory usage per frequency point for both presented application examples. Both our novel method and the one proposed in [26] used a single core on a machine with 3.0 GHz CPU and 16 GB of RAM. In the first application example of Fig. 15, our method exhibits a computation time comparable to [26], albeit with an increase in peak memory usage. Nevertheless, the additional computational steps, and hence memory usage, render our approach applicable to a much broader range of scenarios. The MIMcap example of Fig. 19 demonstrates the versatility of the method and it should be noted that around 80% of the computation time is spent to construct the Green's function matrix for the outside problem, something for which numerous optimization techniques have been proposed in literature. Consequently, further computational performance improvements are feasible.

VII. CONCLUSION

In this work, we proposed a novel differential surface admittance operator for the accurate modeling of complex, piecewise homogeneous cuboidal structures. First, we derived the operator for a piecewise homogeneous cuboid. Second, we tackled general rectilinear polyhedra with a single material interface. Third, we discussed how these formulations are readily extended to allow an arbitrary amount of material interfaces. In a final step, the DSA operator expressed in entire domain basis functions is transformed to local rooftop functions, allowing seamless integration with the EFIE to solve the outside problem.

We provided a thorough numerical validation, comparing our proposed method with state-of-the-art solvers. During this validation, it was shown that our novel method is both accurate and efficient for a broad range of material types. Moreover, practical interconnect examples, e.g., a planar metal-insulator-metal capacitor structure, were provided to illustrate our proposed method's ability to accurately simulate state-of-the-art on-chip topologies.

Note that the presented work focused on the interior problem. Extensions to the exterior problem, e.g., embedding objects into layered media and accelerating the solution via the Fast Multipole Method (FMM) or Adaptive Cross Approximation (ACA), leveraging well-established methods, are a part of future development.

APPENDIX A
ANALYTICAL EXPRESSIONS FOR THE BASIS TRANSFORMS

As mentioned in Section III, the inner products (27) and (28) have an analytical solution, which we provide here. Moreover, the keen reader will observe that the standard analytical expressions contain a denominator which can become zero for certain parameter combinations. These special cases also have an analytical solution that is derived using standard limit evaluation techniques. As in Section III, here we also consider EDBFs depending on the y- and z-coordinates, but the resulting expressions can be extended to other orientations in a straightforward manner.

A. First Basis Transform

The first basis transform is determined by the inner product (27) with its standard analytical solution provided by:

$$c_{n_2' p_2' n_2 p_2} = \langle \mathbf{g}^c_{n_2', p_2'}, \mathbf{g}_{n_2, p_2} \rangle_c = \alpha_1 \beta_1 \gamma_1, \tag{50}$$

$$\alpha_1 = \frac{4 n_2' l_{z_1}^2 l_{y_2} l_{y_1} p_2}{\pi^2 ((n_2' l_{y_2})^2 - (n_2 l_{y_1})^2)((p_2 l_{z_1})^2 - (p_2' l_{z_2})^2)} \tag{51}$$

$$\beta_1 = \sin\left(\frac{\pi y_1 n_2}{l_{y_2}}\right) \times \left((-1)^{n_2'} \sin\left(\frac{\pi z_0 p_2}{l_{z_2}}\right) - (-1)^{n_2' + p_2'} \sin\left(\frac{\pi z_1 p_2}{l_{z_2}}\right)\right) \tag{52}$$

$$\gamma_1 = \sin\left(\frac{\pi y_0 n_2}{l_{y_2}}\right) \times \left((-1)^{p_2'} \sin\left(\frac{\pi z_1 p_2}{l_{z_2}}\right) - \sin\left(\frac{\pi z_0 p_2}{l_{z_2}}\right)\right), \tag{53}$$

The following cases encompass all relevant special cases in which the denominator of (51) can become zero:

$$\lim_{n_2'\to\frac{l_{y_2}n_2}{l_{y_1}}}\langle \mathbf{g}^c_{n_2',p_2'},\mathbf{g}_{n_2,p_2}\rangle_c=\delta_0\varepsilon_0\zeta_0 \tag{54}$$

$$\lim_{n_2',n_2\to 0}\langle \mathbf{g}^c_{n_2',p_2'},\mathbf{g}_{n_2,p_2}\rangle_c=0 \tag{55}$$

$$\lim_{p_2'\to\frac{l_{z_2}p_2}{l_{z_1}}}\langle \mathbf{g}^c_{n_2',p_2'},\mathbf{g}_{n_2,p_2}\rangle_c=\delta_1\varepsilon_1\zeta_1 \tag{56}$$

$$\lim_{p_2',p_2\to 0}\langle \mathbf{g}^c_{n_2',p_2'},\mathbf{g}_{n_2,p_2}\rangle_c=2\pi p_2 l_{z_1}\delta_1\zeta_1 \tag{57}$$

$$\lim_{\substack{n_2'\to\frac{l_{y_2}n_2}{l_{y_1}}\\ p_2'\to\frac{l_{z_2}p_2}{l_{z_1}}}}\langle \mathbf{g}^c_{n_2',p_2'},\mathbf{g}_{n_2,p_2}\rangle_c=\frac{\varepsilon_0\varepsilon_1}{4\pi^2 p_2 n_2 l_{y_2} l_{z_2}} \tag{58}$$

$$\lim_{\substack{n_2'\to\frac{l_{y_2}n_2}{l_{y_1}}\\ p_2',p_2\to 0}}\langle \mathbf{g}^c_{n_2',p_2'},\mathbf{g}_{n_2,p_2}\rangle_c=\frac{l_{z_1}\varepsilon_0}{2\pi n_2 l_{y_2} l_{z_2}} \tag{59}$$

$$\lim_{\substack{n_2',n_2\to 0\\ p_2'\to\frac{l_{z_2}p_2}{l_{z_1}}}}\langle \mathbf{g}^c_{n_2',p_2'},\mathbf{g}_{n_2,p_2}\rangle_c=0 \tag{60}$$

$$\delta_0=\frac{p_2 l_{z_1}^2}{\pi^2 n_2 l_{y_2}((p_2 l_{z_1})^2-(p_2' l_{z_2})^2)} \tag{61}$$

$$\begin{aligned}\varepsilon_0=&2\pi n_2 l_{y_1}\cos(\frac{\pi y_0 n_2}{l_{y_2}})+l_{y_2}\sin(\frac{\pi y_0 n_2}{l_{y_2}})\\ &-l_{y_2}\sin(\frac{\pi(y_0+2l_{y_1})n_2}{l_{y_2}})\end{aligned} \tag{62}$$

$$\zeta_0=(-1)^{p_2'}\sin(\frac{\pi z_1 p_2}{l_{z_2}})-\sin(\frac{\pi z_0 p_2}{l_{z_2}}) \tag{63}$$

$$\delta_1=\frac{n_2' l_{y_1} l_{y_2}}{\pi^2 p_2 l_{z_2}((n_2 l_{y_1})^2-(n_2' l_{y_2})^2)} \tag{64}$$

$$\begin{aligned}\varepsilon_1=&2\pi p_2 l_{z_1}\cos(\frac{\pi z_0 p_2}{l_{z_2}})-l_{z_2}\sin(\frac{\pi z_0 p_2}{l_{z_2}})\\ &+l_{z_2}\sin(\frac{\pi(z_0+2l_{z_1})p_2}{l_{z2}})\end{aligned} \tag{65}$$

$$\zeta_1=(-1)^{n_2'}\sin(\frac{\pi y_1 n_2}{l_{y_2}})-\sin(\frac{\pi y_0 n_2}{l_{y_2}}) \tag{66}$$

B. Second Basis Transform

The analytical expressions for the second inner product (28) are found by performing similar calculations. The results are given below:

$$d_{n_2''p_2''n_2p_2}=\langle \mathbf{g}^d_{n_2',p_2'},\mathbf{g}_{n_2,p_2}\rangle_d=\alpha_2\beta_2\gamma_2, \tag{67}$$

$$\alpha_2=\frac{1}{\pi^2(n_2''^2-n_2^2)(p_2''^2-p_2^2)} \tag{68}$$

$$\begin{aligned}\beta_2=&(n_2''+n_2)(\sin(\frac{(n_2''-n_2)\pi y_0}{l_{y_2}})-\sin(\frac{(n_2''-n_2)\pi y_1}{l_{y_2}}))\\ &-(n_2''-n_2)(\sin(\frac{(n_2''+n_2)\pi y_0}{l_{y_2}})-\sin(\frac{(n_2''+n_2)\pi y_1}{l_{y_2}}))\end{aligned} \tag{69}$$

$$\begin{aligned}\gamma_2=&(p_2''+p_2)(\sin(\frac{(p_2''-p_2)\pi z_0}{l_{z_2}})-\sin(\frac{(p_2''-p_2)\pi z_1}{l_{z_2}}))\\ &+(p_2''-p_2)(\sin(\frac{(p_2''+p_2)\pi z_0}{l_{z_2}})-\sin(\frac{(p_2''+p_2)\pi z_1}{l_{z_2}})).\end{aligned} \tag{70}$$

Just as for the first basis transform, the denominator of (68) becomes zero when $n_1=n_2$ and/or $p_1=p_2$. The following equations cover all these relevant special cases:

$$\lim_{n_2''\to n_2}\langle \mathbf{g}^d_{n_2',p_2'},\mathbf{g}_{n_2,p_2}\rangle_d=\delta_3\varepsilon_3\gamma_2 \tag{71}$$

$$\lim_{n_2'',n_2\to 0}\langle \mathbf{g}^d_{n_2',p_2'},\mathbf{g}_{n_2,p_2}\rangle_d=0 \tag{72}$$

$$\lim_{p_2''\to p_2}\langle \mathbf{g}^d_{n_2',p_2'},\mathbf{g}_{n_2,p_2}\rangle_d=\delta_4\varepsilon_4\beta_2 \tag{73}$$

$$\lim_{p_2'',p_2\to 0}\langle \mathbf{g}^d_{n_2',p_2'},\mathbf{g}_{n_2,p_2}\rangle_d=\delta_4\beta_2 2\pi p_2(z_0-z_1) \tag{74}$$

$$\lim_{\substack{n_2''\to n_2\\ p_2''\to p_2}}\langle \mathbf{g}^d_{n_2',p_2'},\mathbf{g}_{n_2,p_2}\rangle_d=\frac{\varepsilon_3\varepsilon_4}{\pi^2 n_2 l_{y_2} p_2 l_{z_2}} \tag{75}$$

$$\lim_{\substack{n_2''\to n_2\\ p_2'',p_2\to 0}}\langle \mathbf{g}^d_{n_2',p_2'},\mathbf{g}_{n_2,p_2}\rangle_d=\frac{\varepsilon_3(z_0-z_1)}{\pi n_2 l_{y_2} l_{z_2}} \tag{76}$$

$$\lim_{\substack{n_2'',n_2\to 0\\ p_2''\to p_2}}\langle \mathbf{g}^d_{n_2',p_2'},\mathbf{g}_{n_2,p_2}\rangle_d=0 \tag{77}$$

$$\delta_3=\frac{1}{\pi^2 n_2 l_{y_2}(p_2''^2-p_2^2)} \tag{78}$$

$$\begin{aligned}\varepsilon_3=&\frac{l_{y_2}}{2}(\sin(\frac{2\pi y_1 n_2}{l_{y_2}})-\sin(\frac{2\pi y_0 n_2}{l_{y_2}}))\\ &+\pi n_2(y_0-y_1)\end{aligned} \tag{79}$$

$$\delta_4=\frac{1}{\pi^2 p_2 l_{z2}(n_2''^2-n_2^2)} \tag{80}$$

$$\begin{aligned}\varepsilon_4=&\frac{l_{z_2}}{2}(\sin(\frac{2\pi y_0 p_2}{l_{z_2}})-\sin(\frac{2\pi y_1 p_2}{l_{z_2}}))\\ &+\pi p_2(z_0-z_1)\end{aligned} \tag{81}$$

REFERENCES

[1] E. Bogatin, *Signal and Power Integrity–simplified*, ser. Prentice Hall PTR Signal Integrity Library. Prentice Hall, 2010.

[2] J. L. Volakis, A. Chatterjee, and L. C. Kempel, *Finite Element Method Electromagnetics: Antennas, Microwave Circuits, and Scattering Applications*. Wiley-IEEE Press, 1998.

[3] M. Al-Qedra, J. Aronsson, and V. Okhmatovski, "A novel skin-effect based surface impedance formulation for broadband modeling of 3-D interconnects with electric field integral equation," *IEEE Trans. Microw. Theory Techn.*, vol. 58, no. 12, pp. 3872–3881, 2010.

[4] S. Omar and D. Jiao, "A new volume integral formulation for broadband 3-D circuit extraction in inhomogeneous materials with and without external electromagnetic fields," *IEEE Trans. Microw. Theory Techn.*, vol. 61, no. 12, pp. 4302–4312, 2013.

[5] O. Goni and V. I. Okhmatovski, "Exact solution of new magnetic current based surface-volume-surface EFIE and analysis of its spectral properties," *IEEE J. Multiscale and Multiphys. Comput. Techn.*, vol. 7, pp. 102–116, 2022.

[6] A. Ruehli, "Equivalent circuit models for three-dimensional multiconductor systems," *IEEE Trans. Microw. Theory Techn.*, vol. 22, no. 3, pp. 216–221, 1974.

[7] A. Ruehli and H. Heeb, "Circuit models for three-dimensional geometries including dielectrics," *IEEE Trans. Microw. Theory Techn.*, vol. 40, no. 7, pp. 1507–1516, 1992.

[8] A. J. Poggio and E. K. Miller, *Integral Equation Solutions of Three-Dimensional Scattering Problems*. New York, NY, USA: Pergamon, 1973.
[9] J. Peeters, I. Bogaert, and D. De Zutter, "Calculation of MoM interaction integrals in highly conductive media," *IEEE Trans. Antennas Propag.*, vol. 60, no. 2, pp. 930–940, 2012.
[10] M. Gossye, M. Huynen, D. Vande Ginste, D. De Zutter, and H. Rogier, "A Calderón preconditioner for high dielectric contrast media," *IEEE Trans. Antennas Propag.*, vol. 66, no. 2, pp. 808–818, 2018.
[11] P. Yla-Oijala, J. Markkanen, S. Jarvenpaa, and S. P. Kiminki, "Surface and volume integral equation methods for time-harmonic solutions of maxwell's equations," *Progr. Electromagn. Res.*, vol. 149, pp. 15–44, 2014.
[12] P. Yla-Oijala, S. Kiminki, K. Cools, F. Andriulli, and S. Jarvenpaa, "Mixed discretization schemes for electromagnetic surface integral equations," *Int. J. of Numer. Model.: Electron. Netw., Devices Fields*, vol. 25, no. 5-6, pp. 468–483, 2012.
[13] T. B. A. Senior and J. L. Volakis, *Approximate Boundary Conditions in Electromagnetics (Electromagnetics and Radar)*. Edison, NJ, USA: IET, 1995.
[14] D.-S. Wang, "Limits and validity of the impedance boundary condition on penetrable surfaces," *IEEE Trans. Antennas Propag.*, vol. 35, no. 4, pp. 453–457, 1987.
[15] Z. G. Qian, W. C. Chew, and R. Suaya, "Generalized impedance boundary condition for conductor modeling in surface integral equation," *IEEE Trans. Microw. Theory Techn.*, vol. 55, no. 11, pp. 2354–2364, 2007.
[16] W. C. C. Zhiguo Qian, Mei Song Tong, "Conductive medium modeling with an augmented GIBC formulation," *Progr. Electromagn. Res.*, vol. 99, pp. 261–272, 2009.
[17] D. De Zutter and L. Knockaert, "Skin effect modeling based on a differential surface admittance operator," *IEEE Trans. Microw. Theory Techn.*, vol. 53, no. 8, pp. 2526–2538, 2005.
[18] U. R. Patel, B. Gustavsen, and P. Triverio, "Proximity-aware calculation of cable series impedance for systems of solid and hollow conductors," *IEEE Trans. Power Del.*, vol. 29, no. 5, pp. 2101–2109, 2014.
[19] U. R. Patel and P. Triverio, "Skin effect modeling in conductors of arbitrary shape through a surface admittance operator and the contour integral method," *IEEE Trans. Microw. Theory Techn.*, vol. 64, no. 9, pp. 2708–2717, 2016.
[20] X. Zhou, Z. Zhu, and S. Yang, "Formulation of single-source surface integral equation for electromagnetic analysis of 2D partially connected penetrable objects," *IEEE J. Multiscale and Multiphys. Comput. Techn.*, vol. 6, pp. 16–23, 2021.
[21] D. Bosman, M. Huynen, D. De Zutter, X. Sun, N. Pantano, G. Van der Plas, E. Beyne, and D. Vande Ginste, "Efficient characterization of interconnects with arbitrary polygonal cross sections using Fokas-derived Dirichlet-to-Neumann operators," *IEEE Trans. Compon. Packag. Manuf. Technol.*, vol. 13, no. 10, pp. 1567–1575, 2023.
[22] D. Bosman, M. Huynen, D. De Zutter, X. Sun, N. Pantano, G. Van der Plas, E. Beyne, and D. Vande Ginste, "Analysis and application of a surface admittance operator for combined magnetic and dielectric contrast in emerging interconnect topologies," *IEEE Trans. Microw. Theory Techn.*, vol. 71, no. 7, pp. 2794–2806, 2023.
[23] M. Huynen, M. Gossye, D. De Zutter, and D. Vande Ginste, "A 3-D differential surface admittance operator for lossy dipole antenna analysis," *IEEE Antennas Wireless Propag. Lett.*, vol. 16, pp. 1052–1055, 2017.
[24] M. Huynen, D. De Zutter, and D. Vande Ginste, "Boundary integral equation study of the influence of finite conductivity on antenna radiation using a 3-D differential surface admittance operator," in *Proc. Int. Appl. Comput. Electromagn. Soc. Symp. (ACES)*, mar. 2017, pp. 1–2.
[25] M. Huynen, D. De Zutter, and D. Vande Ginste, "Rigorous full-wave resistance and inductance computation of 3-D interconnects," *IEEE Microw. Wireless Compon. Lett.*, vol. 28, no. 6, pp. 455–457, 2018.
[26] M. Huynen, K. Y. Kapusuz, X. Sun, G. Van der Plas, E. Beyne, D. De Zutter, and D. Vande Ginste, "Entire domain basis function expansion of the differential surface admittance for efficient broadband characterization of lossy interconnects," *IEEE Trans. Microw. Theory Techn.*, vol. 68, no. 4, pp. 1217–1233, 2020.
[27] U. R. Patel, S. Sharma, S. Yang, S. V. Hum, and P. Triverio, "Full-wave electromagnetic characterization of 3D interconnects using a surface integral formulation," in *Proc. IEEE 26th Conf. Elect. Perform. Electron. Packag. Syst.*, oct. 2017, pp. 1–3.
[28] U. R. Patel, P. Triverio, and S. V. Hum, "A single-source surface integral equation formulation for composite dielectric objects," in *Proc. IEEE Int. Symp. Antennas Propag. & USNC/URSI Nat. Radio Sci. Meeting*, Jul. 2017, pp. 1453–1454.
[29] P. Ylä-Oijala, S. P. Kiminki, J. Markkanen, and S. Järvenpää, "Error-controllable and well-conditioned MoM solutions in computational electromagnetics: ultimate surface integral-equation formulation [open problems in cem]," *IEEE Antennas Propag. Mag.*, vol. 55, no. 6, pp. 310–331, 2013.
[30] T. Hughes, J. Cottrell, and Y. Bazilevs, "Isogeometric analysis: CAD, finite elements, NURBS, exact geometry and mesh refinement," *Comput. Methods Appl. Mech. Eng.*, vol. 194, no. 39, pp. 4135–4195, 2005.
[31] D. Bosman, M. Huynen, D. De Zutter, and D. Vande Ginste, "Construction of the differential surface admittance operator with an extended Fokas method for electromagnetic scattering at polygonal objects with arbitrary material parameters," *Comput. Math. Appl.*, vol. 128, pp. 44–54, 2022.
[32] R. F. Harrington, "Boundary integral formulations for homogeneous material bodies," *J. Electromagn. Waves Appl.*, vol. 3, no. 1, pp. 1–15, 1989.
[33] Z.-G. Qian and W. C. Chew, "Fast full-wave surface integral equation solver for multiscale structure modeling," *IEEE Trans. Antennas Propag.*, vol. 57, no. 11, pp. 3594–3601, 2009.
[34] Dassault Systèmes, *CST Studio Suite*, 2024, https://www.3ds.com/products-services/simulia/products/cst-studio-suite.
[35] H. Lin, D. Velenis, P. Nolmans, X. Sun, F. Catthoor, R. Lauwereins, G. Van der Plas, and E. Beyne, "84%-efficiency fully integrated voltage regulator for computing systems enabled by 2.5-D high-density MIM capacitor," *IEEE Trans. VLSI Syst.*, vol. 30, no. 5, pp. 661–665, 2022.
[36] D. Kannadassan, K. Sivasankaran, S. Kumaravel, C.-H. Cheng, M. S. Baghini, and P. S. Mallick, "High-k metal–insulator–metal capacitors for RF and mixed-signal VLSI circuits: Challenges and opportunities," *Proc. IEEE*, vol. 112, no. 10, pp. 1610–1631, 2024.
[37] P.-Y. Chiu and M.-D. Ker, "Metal-layer capacitors in the 65nm CMOS process and the application for low-leakage power-rail ESD clamp circuit," *Microelectron. Reliab.*, vol. 54, no. 1, pp. 64–70, 2014.
[38] C. Roda Neve, M. Detalle, P. Nolmans, Y. Li, J. De Vos, G. Van der Plas, G. Beyer, and E. Beyne, "High-density and low-leakage novel embedded 3D MIM capacitor on Si interposer," in *Proc. IEEE Int. 3D Syst. Integr. Conf. (3DIC)*, Sep. 2016, pp. 1–4.

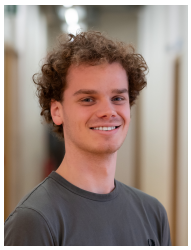

Tim Pattyn (Student Member, IEEE) received the M.Sc. degree in electrical engineering from Ghent University, Ghent, Belgium, in 2023.

He is currently pursuing the Ph.D. degree in electrical engineering with the research group Quest/IDLab, Department of Information Technology, at Ghent University—imec. His research interests lie in the field of computational electromagnetics, with a particular focus on boundary integral equation methods. His work addresses applications in interconnect modeling, electromagnetic compatibility (EMC) analysis, and the signal integrity (SI), power integrity (PI), and EMC-aware design of interconnects.

He received the Best Student Paper Award at the 2024 IEEE Workshop on Signal and Power Integrity (SPI).

Xiao Sun (Member, IEEE) received the Ph.D. degree in electrical engineering from Université Grenoble Alpes, Grenoble, France, in 2001.

She is currently a Principal Member of Technical Staff with imec, Leuven, Belgium. She has (co)authored over 70 peer-reviewed journals and conference papers and one book chapter. Her research interests include RF design, modeling, and characterization for 3-D interconnects and their impact on 3-D integrated circuits (ICs), heterogeneous integration, and packaging for RF and 5G applications.

Dr. Sun was a recipient of the prestigious Outstanding Session Paper Award from the IEEE Electronic Components and Technology Conference (ECTC) 2015.

Eric Beyne (Senior Member, IEEE) received the master's degree in electrical engineering and the Ph.D. degree in applied sciences from KU Leuven, Leuven, Belgium, in 1983 and 1990, respectively.

Since 1986, he has been with imec, Leuven, where he has been involved in advanced packaging and interconnect technologies. He is currently a Senior Fellow with imec, where he is the Program Director of the 3-D System Integration Program.

Daniël De Zutter (Life Fellow, IEEE) was born in 1953. He received the M.Sc. degree in electrical engineering, and the Ph.D. degree and the degree equivalent to the German Habilitation degree from the University of Ghent, Ghent, Belgium, in 1976, 1981, and 1984, respectively.

He was a Full Professor of electromagnetics. From 2004 to 2008, he was the Dean of the Faculty of Engineering, Ghent University, where he was the Head of the Department of Information Technology, from 2010 to 2016. His research focusses on all aspects of circuit and electromagnetic modeling of high-speed and high-frequency interconnections and packaging, electromagnetic compatibility (EMC), and numerical solutions of Maxwell's equations. He is the author or coauthor of more than 220 international journal articles (cited in the Web of Science) and 250 articles in conference proceedings.

Dr. De Zutter was an Associate Editor of the IEEE TRANSACTIONS ON MICROWAVE THEORY AND TECHNIQUES.

Martijn Huynen (S'18 - M'19) received the M.Sc. degree and Ph.D. degree in electrical engineering from Ghent University, Gent, Belgium in 2014 and 2019, respectively. From May to July 2023, he was a Visiting Scientist with the Department of Electrical and Computer Engineering, University of Manitoba, Winnipeg, Canada.

He is currently an Assistant Professor at the Research Lab Quest/IDLab in the Department of Information Technology of Ghent University/imec. His research focuses on computational electromagnetics, more specifically boundary integral equations, with applications in interconnect modeling, electromagnetic compatibility analysis and antenna design.

Dr. Huynen received the Best Student Paper Award at the 2017 Applied Computational Electromagnetics Society (ACES) Symposium.

Dries Vande Ginste (Senior Member, IEEE) received the M.Sc. degree and the Ph.D. degree in electrical engineering from Ghent University, Gent, Belgium, in 2000 and 2005, respectively. He is currently an Associate Professor with Ghent University and imec, heading the research lab quest.

In June and July 2004, he was a Visiting Scientist with the Department of Electrical and Computer Engineering, University of Illinois Urbana-Champaign, Champaign, IL, USA. From September to November 2011, he was a Visiting Professor with the EMC Group, Dipartimento di Elettronica, Politecnico di Torino, Turin, Italy. He has authored or coauthored more than 200 papers in international journals and in conference proceedings. His research interests include computational quantum mechanics and electromagnetics, electromagnetic compatibility, signal and power integrity.

Dr. Vande Ginste was the recipient of the International Union of Radio Science Young Scientist Award at the 2011 URSI General Assembly and Scientific Symposium, the Best Poster Paper Award at the 2012 IEEE Electrical Design of Advanced Packaging and Systems Symposium (EDAPS), the Best Paper Award at the 2013 IEEE Workshop on Signal and Power Integrity (SPI), the Best Paper Award at the 2013 IEEE International Conference on Electrical Performance of Electronic Packaging and Systems, and the Best Paper Award at the 2016 IEEE Electrical Design of Advanced Packaging and Systems Symposium. He was the Chair of the 2014 IEEE Workshop on Signal and Power Integrity. He is an Associate Editor for IEEE Transactions on Signal and Power Integrity.